Mechanics of Materials 80 (2015) 67–86

Contents lists available at ScienceDirect

Mechanics of Materials

journal homepage: www.elsevier.com/locate/mechmat

On the modeling of the thermo-mechanical responses of four different classes of NiTi-based shape memory materials using a general multi-mechanism framework

A.F. Saleeb [a,*], B. Dhakal [a], S. Dilibal [a], J.S. Owusu-Danquah [a], S.A. Padula II [b]

[a] Department of Civil Engineering, The University of Akron, Akron, OH 44325-3905, USA
[b] N.A.S.A. Glenn Research Center, 21000 Brookpark Rd., Cleveland, OH 44135, USA

ARTICLE INFO

Article history:
Received 25 February 2014
Received in revised form 4 August 2014
Available online 5 October 2014

Keywords:
NiTi shape memory alloys
Material modeling
Superelastic behavior
Pseudoplastic behavior
Evolution
Thermal cycles

ABSTRACT

The properties of a shape memory alloy (SMA) have been shown to be highly dependent on the chemical composition and thermo-mechanical processing applied to the material. These differences dictate the degree of superelasticity, pseudoplasticity, shape memory effect, and evolution under mechanical/thermal loading cycles, that is observed in the material. Understanding and utilizing these unique phenomena has become essential in many engineering applications. It is, therefore, important to provide two key ingredients in any SMA constitutive model; (i) a sufficiently comprehensive scope in the mathematical formulation to handle different classes of SMA materials; and (ii) a *general* model parameterization derived from fundamental tests that can be used for a specific SMA as intended for use in a given application. The present work is aimed at a detailed investigation of the interaction aspects between the above items (i) and (ii) in the context of using a recent three-dimensional, multimechanism-based SMA framework to model the experimentally measured responses of four different classes of SMA materials: (a) a commercial superelastic NiTi, (b) a powder metallurgically-processed NiTi-based SMA material, (c) a commercial $Ni_{49.9}Ti_{50.1}$ actuation material, and (d) a high-temperature $Ni_{50.3}Ti_{29.7}Hf_{20}$ alloy. To facilitate the parameterization task, the model parameters are classified into two groups, i.e., (1) fixed parameters that are designed to capture the non-linear, hysteretic response under any thermo-mechanical loading condition, and (2) a set of functionally dependent material parameters which account for a number of refinements including asymmetry in tension and compression responses, temperature- and stress-state dependencies, etc. The results of the work showed that the complexity of the characterization is dependent on the SMA feature exploited by the specific application intended, which in turn dictates the amount and type of test data required to accurately predict a given application response.

1. Introduction

It is well known that SMA materials are very sensitive to the chemical composition, thermo-mechanical processing (hot/cold working and heat treatment), and applied stress conditions (Otsuka and Wayman, 1998). For this reason, the metallurgical and experimental history of the SMA material plays a vital role in determining the unique properties that are observed, such as superelasticity, pseudoplasticity, shape memory effect, and evolutionary behavior.

The aforementioned sensitivity to processing/loading conditions can be used to one's advantage to obtain the most convenient properties for any specific application.

* Corresponding author. Tel.: +1 330 972 7692; fax: +1 330 972 6020.
E-mail address: saleeb@uakron.edu (A.F. Saleeb).

http://dx.doi.org/10.1016/j.mechmat.2014.09.001
0167-6636/

For instance, Ni-rich NiTi compositions (more than 50.5% at. Ni) have lower transformation temperatures than their Ti-rich counterparts. This lower transformation temperature facilitates the use of the superelastic property which is appropriate for biomedical stent applications at constant body temperature (Gall et al., 2005). Moreover, aging of a Ni-rich alloy enhances cyclic stability (Coughlin et al., 2012; Evirgen et al., 2012; Yawny et al., 2008). On the other hand, the NiTi-based ternary alloys with the addition of Hf exhibit a dramatic increase in the transformation temperature (Angst et al., 1995; Kockar et al., 2006), thus rendering this material suitable for high-temperature actuation applications in the aerospace field. As can be seen by the aforementioned, the different engineering or medical SMA-based applications are designed to exploit a specific shape memory behavior such as superelasticity (SE), one-way shape memory effect (OWSME), or stress-assisted two-way shape memory effect (TWSME).

The characteristic response of a particular SMA can only be unveiled through the comprehensive characterization of the SMA by conducting a detailed set of experiments under different mechanical as well as thermal loading scenarios. Due to constraints on time, cost, expertise, etc., access to such information is very rare. Hence, there is a need for a systematic, comprehensive set of experimental works that provides the appropriate information regarding the SMA behavior to be exploited in the application. Once the application based experiments are carried out, with relevant and appropriate test procedures, the designers/engineers face the dilemma of selecting an appropriate material model from the many choices available in the literature. As discussed in the recent publication by Hartl et al. (2010), this is particularly difficult since most of the available models require the use of test data for stabilized/trained materials but do not specify the nature of the training procedure. In particular, it is known that the behavior of a trained SMA material is dictated by the specific for a given load condition, and once that load condition is changed, the material will re-initiate stages of transient changes and subsequent evolution of deformation. Hence, there is a vital need for a general SMA material formulation, which once formulated, can be used by designers/engineers for the analysis of various intended applications using different classes of SMA materials, regardless of prior thermomechanical history. A general discussion of the different constitutive modeling approaches for SMA materials can be found in Lagoudas et al. (2006), Patoor et al. (2006), Kan and Kang (2010) and Saleeb et al. (2011).

In the work presented here, a general SMA modeling strategy (developed by Saleeb et al. (2011)) will be specialized to handle four different classes of SMA materials. Note that two of these materials (55NiTi ($Ni_{49.9}Ti_{50.1}$) and superelastic $Ni_{50.7}Ti_{49.3}$) are among the most-widely-used in applications and are commercially available. The other two material systems (i.e., ternary $Ni_{50.3}Ti_{29.7}Hf_{20}$ for aerospace applications and the powder metallurgically processed NiTi SMA system for biomedical applications) are representative of "state-of-the-art" materials being developed to enhance the material properties. Furthermore, the widely different response characteristic of these four materials presents an excellent setting to evaluate the viability of the developed modeling framework for use in applications. To facilitate the model parameterization for the four materials, we utilize the ability to activate or deactivate the temperature/stress functional dependency of the underlying inelastic mechanisms in the general framework. It will be shown that drastically different material responses, required to predict specific applications can be easily manifested through altering the framework's parameterization and that the complexity/simplicity of the parameterization is commensurate with the complexity of the deformation behavior being exploited. Hence, the parameterization will be shown to be quite complex for the applications requiring thermal actuation behavior (as in the cases of the commercially available $Ni_{49.9}Ti_{50.1}$ (at.%), and the high-temperature $Ni_{50.3}Ti_{29.7}Hf_{20}$ alloy (at.%)) but can be extremely simplified to handle simpler cases such as superelastic deformation of a stent.

To better place into perspective the scope, overall objectives, and practical utility of the present multimechanism model and its characterization presented here, we use the schematics of Fig.1. More specially, an application-driven approach is adopted, where the following observation is emphasized. Each technologically-significant application exploits one or more of the SMA response characteristics (see 1st row in Fig. 1), typically involving a complex initial/boundary-value problem (see 2nd row in Fig. 1), such as the cases of biomedical stents and different configurations of solid-state actuators. Hence, the *mathematical* formulations and assumptions made in the establishment of this model account for multi-axiallity and are sufficiently *comprehensive* in scope to treat *all* these different cases (see 3rd row in Fig. 1). However, for *practical* utility, the model *characterization* is *flexible* enough to allow the use of *reduced* sets of test data (4th row in Fig. 1), commensurate with the *limited* scope of a *specific* application (last row in Fig. 1).

2. Experimental measurements and observations

The investigation was carried out on four different NiTi-based, polycrystalline, SMA materials. These materials are; (a) a commercial $Ni_{49.9}Ti_{50.1}$ (at.%) actuation material, (b) a high-temperature $Ni_{50.3}Ti_{29.7}Hf_{20}$ alloy (at.%), (c) a powder metallurgically processed NiTi based material, and (d) a commercial superelastic NiTi. Details of the specific experimental results for each of these separate materials are given below.

2.1. $Ni_{49.9}Ti_{50.1}$ (at.%) SMA material

Here, an extensive number of isobaric, thermal cycling results for a $Ni_{49.9}Ti_{50.1}$ (at.%) material were utilized. Seven different bias stress levels (10, 50, 80, 100, 150, 200, and 300 MPa) were characterized over 100 thermal cycles (except only 88 cycles are available for 200 MPa) using a temperature range of 30 °C to 165 °C (Padula et al., 2013; Saleeb et al., 2013; Saleeb et al., 2013; Atli et al., 2013). Cylindrical, uniform-gage length tensile specimens with a diameter of 3.81 mm and a reduced gage length of 25.4 mm in the hot-rolled/hot-drawn and hot-straightened

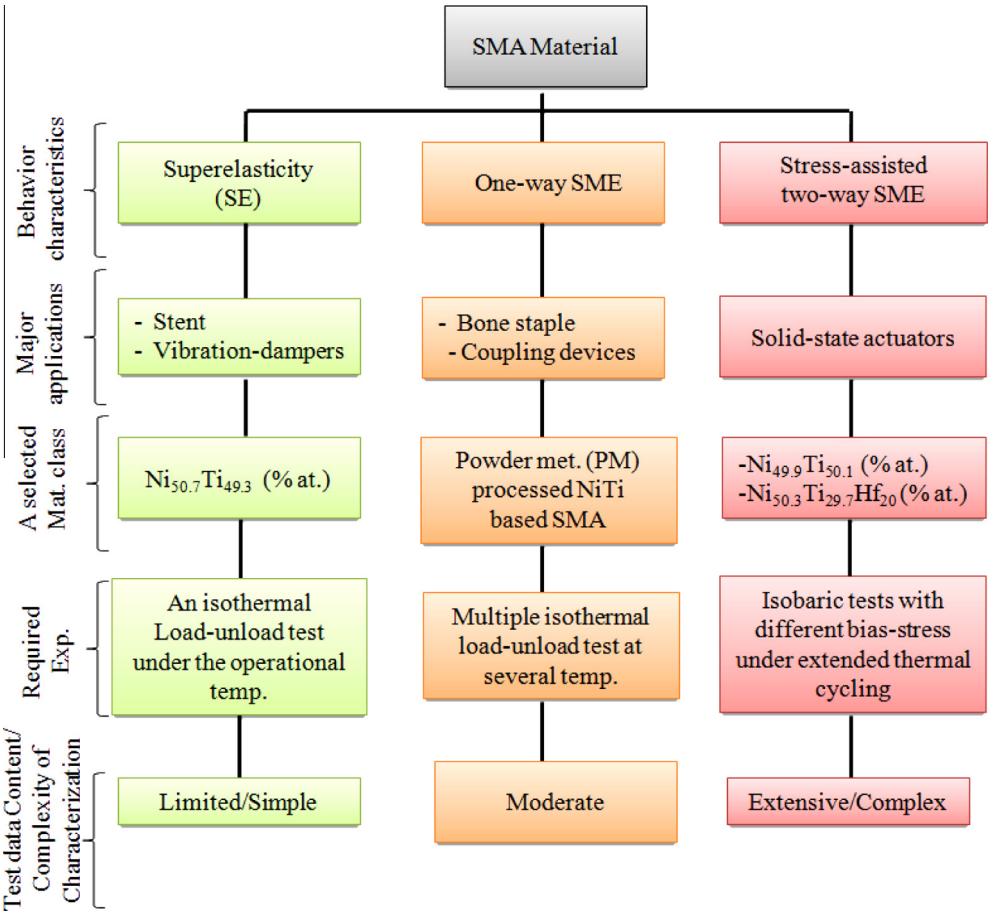

Fig. 1. The *application-driven* approach for developing multi-mechanism model. Each *technologically-significant* application exploits one or more of the SMA response characteristics, typically involving a complex initial/boundary/value problem. Therefore, *mathematical* formulation of the model should account for multi-axiallity and be sufficiently *comprehensive* in scope to treat *all* these cases. However, for *practical* utility, the model *characterization* should be *flexible* to allow the use of *reduced* sets of test data, commensurate with the *limited* scope of a specific application.

condition were utilized for the isobaric thermal cyclic experiments. DSC results for the specimens were $M_f = 47\ ^\circ C$, $M_s = 75\ ^\circ C$, $A_s = 89\ ^\circ C$, and $A_f = 113\ ^\circ C$ under stress-free conditions according to Padula et al. (2012) and Padula et al. (2013).

A typical strain-vs-temperature evolution response plot for 100 thermal cycles under a constant stress level (100 MPa) of the $Ni_{49.9}Ti_{50.1}$ (at.%) material is described in Fig. 2. For convenience, the strain at the martensite (low temperature) side is defined as ε_M and the counterpart strain value at the austenite (high temperature) side is taken as ε_A. In this isobaric test, a virgin specimen is initially loaded in stress-control mode at room temperature in the martensite phase until a bias-stress of 100 MPa is reached, with only a small amount of strain being imparted to the material as a result of this initial loading (path '1'–'2' in Fig. 2(b)). Under this same value of the applied stress, the specimen is heated through the first reverse transformation up to 165 °C. During the first heating (path '2'–'3' in Fig. 2(b)), a slight increase occurs on the strain-temperature curve followed by a decrease, accumulating only a very small amount of strain. Upon cooling to 30 °C (path '3'–'4' in Fig. 2(b)), a significant amount of strain (nearly 3.7%) was accumulated. This strain-vs-temperature response for the first thermal cycle (cycle 1) can be thought of as a *transient*response, as the pattern associated with it is short lived and not repeated until another load excursion has occurred. Each subsequent cycle induces strain evolution (cycle 2–50) until a saturation level is reached and eventually only minor changes are seen in the dimensional evolution upon further cycling (cycle 50–100). This entire set of repeated thermo-mechanical cycles (also known as "training") is called *stress-assisted, two-way shape memory effect* (Wada and Liu, 2008). Since the strain evolution during the thermal cycles is significantly greater than the transient response that is observed in the material, the $Ni_{49.9}Ti_{50.1}$ (at.%) material is considered a *high evolver*.

The solid-state actuators which utilized such materials make use of an actuation stroke (i.e., $\varepsilon_{ACT}^{(n)} = \varepsilon_M^{(n)} - \varepsilon_A^{(n)}$ for the 'nth' thermal cycle) produced during the load-bias thermal cycling. In order to acquire an efficient design and performance, the actuator should display some level of dimensional stability. Ideally, this corresponds to a *stabilized* deformation hysteresis loop during all thermal

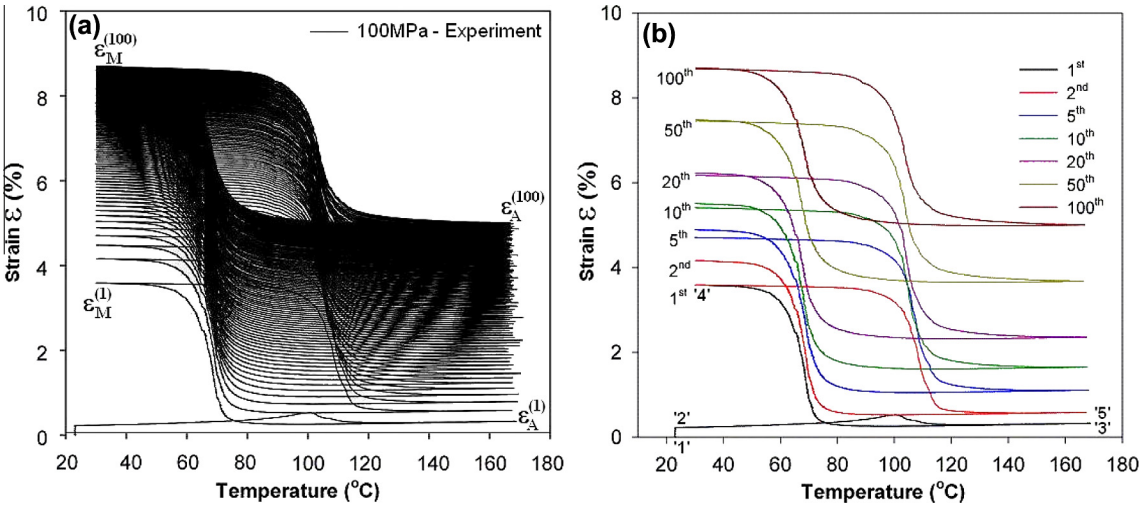

Fig. 2. Experimental strain-vs-temperature isobaric test response of $Ni_{49.9}Ti_{50.1}$ at bias stress of 100 MPa in a temperature range from 30 °C to 165 °C: (a) 100 thermal cycles, and (b) selected cyclic response at initial (1st, 2nd, and 5th) intermediate (10th, 20th to 50th) and later (50th to 100th) thermal cycles (Padula et al., 2013, Saleeb et al., 2013).

cycles with no change in $\varepsilon_M, \varepsilon_A$ and ε_{ACT}. However, from a practical standpoint, this implies an "acceptably" small per-cycle-change in each of these three quantities. Hence, it becomes important to study the cyclic, evolutionary characteristic of the actuation material to assess the effectiveness of any training procedure or thermo-mechanical processing techniques that can be employed to achieve the desirable level of dimensional stability.

2.2. $Ni_{50.3}Ti_{29.7}Hf_{20}$ (at.%) SMA material

$Ni_{50.3}Ti_{29.7}Hf_{20}$ (at.%) tensile specimens taken from two different heat treatments of the material (labeled as Extrusion-124 and Extrusion-146) were used for isobaric experiments. Both extrusions received an aging treatment at 550 °C for 3 hours. Dog-bone specimens with a 5 mm gage diameter and 17.8 mm gage length were machined from both extrusions. For clarity in the following we will refer to these two different cases as Extrusion-124 and Extrusion-146. The DSC results for the specimens indicated M_f= 129 °C, M_s= 136 °C, A_s= 156 °C, and A_f= 165 °C under stress-free conditions (Bigelow et al., 2011 and Noebe, 2012).

These transformation temperatures for $Ni_{50.3}Ti_{29.7}Hf_{20}$ (at.%) material are higher than their counterpart temperatures for $Ni_{49.9}Ti_{50.1}$. More specifically, the M_f = 129 °C for the $Ni_{50.3}Ti_{29.7}Hf_{20}$ is nearly three-times that of the $Ni_{49.9}Ti_{50.1}$, whereas the A_f = 165 °C for the $Ni_{50.3}Ti_{29.7}Hf_{20}$ is approximately 50% more than that of $Ni_{49.9}Ti_{50.1}$. This partly justifies the classifications "high-temperature" and "ordinary" SMA when refering to the use of the $Ni_{50.3}Ti_{29.7}Hf_{20}$ and $Ni_{49.9}Ti_{50.1}$, respectively, in solid-state actuators.

For the specimens taken from Extrusion-146, isobaric tensile tests under different values of bias-stress (80, 150, and 200 MPa) were conducted with 100 thermal cycles between 30 °C and 300 °C (Noebe, 2012). A similar isobaric thermal cycling test procedure to that mentioned in Section 2.1 was used for these tests. The experimental results of one of these isobaric tests (200 MPa bias-stress level) is depicted in Fig. 3(a). The results show that $Ni_{50.3}Ti_{29.7}Hf_{20}$(Extrusion-146) exhibits much less strain evolution during the 100 thermal cycles in comparison with $Ni_{49.9}Ti_{50.1}$. In particular, the changes in strains ε_M and ε_A between the 1st ($\varepsilon_M^{(1)}$ and $\varepsilon_A^{(1)}$) and 100th ($\varepsilon_M^{(100)}$ and $\varepsilon_A^{(100)}$) thermal cycles were nearly 0.3% and 0.1%, respectively (see Fig. 3(a)). This is to be contrasted to the much larger magnitudes obtained for $Ni_{49.9}Ti_{50.1}$. From the standpoint of cyclic stability, this clearly indicates superior performance by $Ni_{50.3}Ti_{29.7}Hf_{20}$ (Extrusion-146). Since the strain evolution during the thermal cycles is significantly lower than the transient response that is observed in the material, the $Ni_{50.3}Ti_{29.7}Hf_{20}$ (at.%) material (Extrusion-146) is considered a *low evolver*.

A more extensive set of test data was available for Extrusion-124. This experimental set consisted of load-biased tests cycled between 30 °C and 300 °C under bias stresses ranging from 0 to 500 MPa (Bigelow et al., 2011 and Noebe, 2012). Both tension and compression were investigated by conducting two thermal cycles at each stress level on the same specimen. This experimental procedure, where each stress in the sequence is performed one after the other, is also known as a "series" load-biased, isobaric test. The results of these load-biased thermal cycles under tension and compression are shown in Fig. 3(b) (Note that only the data from the second cycle at each stress level is plotted in the figure). It is observed that the actuation strain during load-biased thermal cycling increases with increased stress from 1.49% at 100 MPa to 3.69% at 500 MPa under tension and from 1.03% at 100 MPa to 2.75% at 500 MPa in compression. It is clear from the results in Fig. 3(b) that: (a) $Ni_{50.3}Ti_{29.7}Hf_{20}$ (Extrusion-124) material exhibits a strong asymmetry in tension and compression, (b) in both the tension and compression regimes, there is a significant effect on the actuation strain

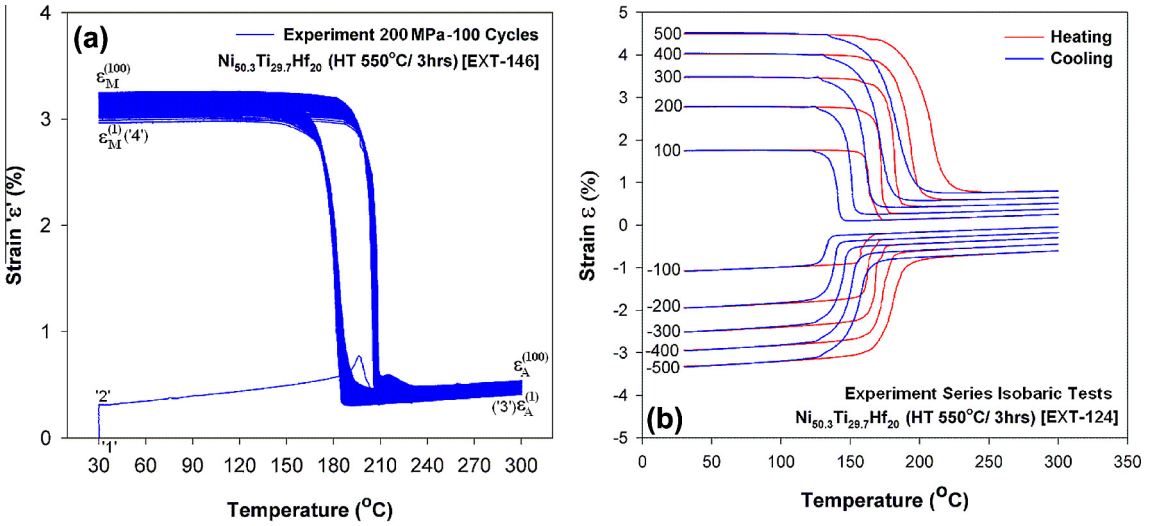

Fig. 3. Experimental strain-vs-temperature response of $Ni_{50.3}Ti_{29.7}Hf_{20}$: (a) isobaric test for Extrusion-146 at bias stress of 200 MPa for 100 cycles in a temperature range from 30 °C to 300 °C; and (b) cyclic response (2nd thermal cycle) for a series isobaric test for Extrusion-124 in tension (from 100 MPa to 500 MPa with increment of 100 MPa) followed by compression (from −100 MPa to −500 MPa with increment of −100 MPa). Fig. 3(a) is courtesy of Dr. R. Noebe (NASA GRC) and Fig. 3(b) is taken from Bigelow et al. (2011).

resulting from changes of the bias-stress magnitude (c) *transformation temperatures* dramatically increase with increases in the magnitude of stress applied.

In order to have a unified material response for the $Ni_{50.3}Ti_{29.7}Hf_{20}$ alloy, the slight differences in deformation behavior observed between specimens taken from Ext 146 and 124 were mitigated as follows. The more extensive set of test data from Ext 124 was used as the typical response that would be observed from such an alloy. In addition, since no extended thermal cycling data was available for this specific extrusion, an *assumption* was made regarding the amount of cyclic strain evolution that would be allowed in the calibrated model. In this case, levels comparable to what was observed for tests conducted on Extrusion 146 were assumed for the purposes of the calibration to be described in Sections 4.2 and 5.2.

Unlike $Ni_{49.9}Ti_{50.1}$solid-state actuators, $Ni_{50.3}Ti_{29.7}Hf_{20}$ actuators are typically intended for use in a higher range of operation temperature. However, all the remarks made at the end of Section 2.1 above regarding the relevance of the cyclic isobaric test results to the assessment of actuator performance also apply here.

2.3. A powder metallurgical processed NiTi SMA material

The experimental test results of this specific case were taken from a powder metallurgically processed material which contains pre-alloyed *NiTi* powder (54.6 wt.%Ni and 45.4 wt.%Ti), with two *p*olymer additives; i.e. amide wax and a polyethylene wax (68 vol.%, 19 vol.%, 13 vol.% respectively) (Krone et al., 2005; Christ and Reese, 2009). For brevity, this material will be referred to here as PM/NiTi-P. The powder metallurgical sintering process was conducted at 1230 °C for 5 h according to Krone et al. (2005). Differential scanning calorimetry (DSC) results for the phase transformation characteristic temperatures indicated the following values: the martensite finish (M_f) temperature = −43 °C, martensite start (M_s) temperature = −23 °C, austenite start (A_s) temperature = −13 °C, and austenite finish (A_f) = 29 °C. The dog-bone, plate-like, tensile specimen utilized in the experiments had dimensions of 2.2 mm × 3.3 mm for its cross-section and 43.7 mm for its length (15.8 mm gauge) (Krone et al., 2005).

The isothermal stress–strain measurements were made at five different temperatures (−48 °C, 13 °C, 37 °C, 50 °C, and 90 °C) as reported in Krone et al. (2005) and Christ and Reese (2009). This includes two load-unload tension tests which were conducted under combined control (strain control to 4% during loading, and stress control to zero stress during unloading) at −48 °C and 37 °C (Fig. 4(a)). In addition, a set of strain-controlled tension tests were conducted to 5% strain without unloading at 13 °C, 50 °C, and 90 °C as shown in Fig. 4(b).

In the load-unload test at −48 °C (below M_f), the loading curve (path '1'–'2'–'3') shows a large and rapid increase of stress to nearly 150 MPa within 0.5% strain, followed by a small additional increase in stress of 50 MPa within an extended range of strain of nearly 3.5%. In the unloading phase of the test, the stress is rapidly decreased to zero recovering a very small amount of strain of nearly 0.4%, thus producing a large magnitude of residual strain (3.6%). This response is termed as pseudoplastic due to the large amount of unrecovered strain. On the other hand, a superelastic response was exhibited for the cyclic test conducted at 37 °C. In terms of the experimental results for 13 °C, 50 °C, and 90 °C, the loading curves which were presented in Fig. 4(b) show an increase of the "plateau" stress magnitude at the end of the apparent linear part of the response curves (corresponding to the small strain range of nearly 0.5%) with increasing test temperature.

The test results given here are intended for a bone staple application that exploits the one-way shape memory

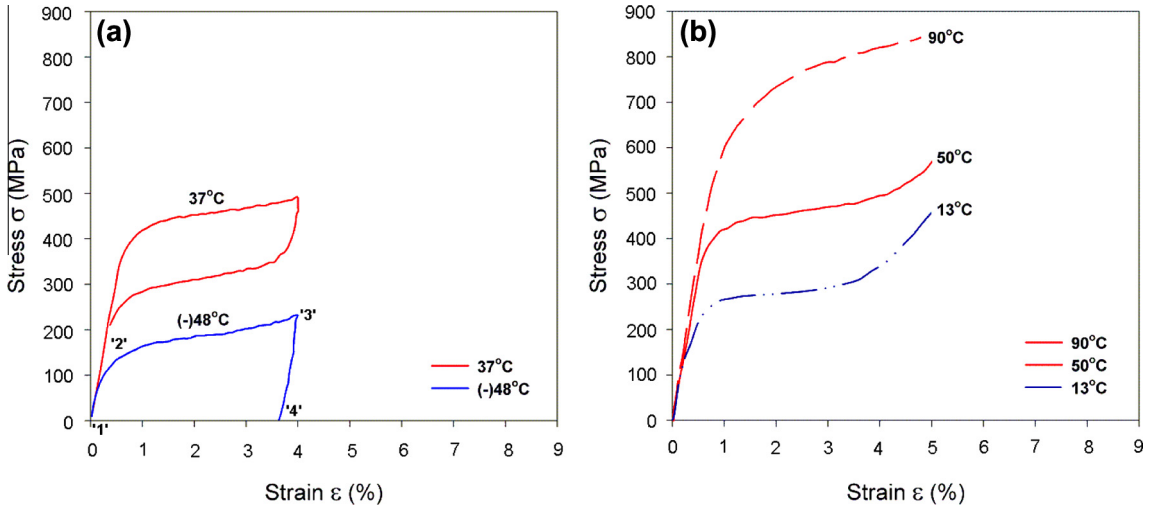

Fig. 4. Experimental stress-vs-strain response of the powder metallurgical processed NiTi material: (a) load-unload curves at 37 °C and −48 °C, under combined control, i.e., strain control during loading to 4% and stress control to zero stress at end of the unload, and (b) loading curves at 90 °C, 50 °C, and 13 °C (Krone et al., 2005;Christ and Reese, 2009).

effect character. In this application, the PM/NiTi-P material undergoes a wide range of temperature changes. In a typical bone stapling procedure, the initial phase involves deforming the staple in the martensite state (−48 °C in the experiment of Krone et al. (2005)). The second phase concerns the development of a large clamping force when the staple legs come into contact with the bone surfaces, which is achieved by heating the staple to 50 °C (above the A_f) as eluded to in Krone et al. (2005). For such a case, it is clear that the characterization of the PM/NiTi-P material must include multiple-temperature experiments as described in Fig. 4.

2.4. A superelastic NiTi SMA material

A $Ni_{50.7}Ti_{49.3}$ (at.%) SMA material was selected to investigate the superelastic SMA behavior, which is appropriate for biomedical applications such as self expending stents. The experimental test results of the commercially available superelastic $Ni_{50.7}Ti_{49.3}$ alloy (at.%) medical grade *wire* with a diameter of 0.5 mm were taken from Liu et al. (2008). Although not all the characteristic temperatures for the present superelastic material were reported in Liu et al. (2008), the specific austenite finish (A_f) temperature was given as 19 °C (lower than body temperature) as measured using differential scanning calorimetry (DSC) under a stress-free condition in this same reference. However, other DSC studies (McNaney et al., 2003) performed on the *very* similar composition of NiTi, i.e., for a $Ni_{50.8}Ti_{49.2}$ (at.%), revealed the following set of the phase transformation temperatures; i.e, $M_f = -87.43$ °C, $M_s = -51.55$ °C, $A_s = -6.36$ °C, and $A_f = 18.13$ °C.

Fig. 5 shows the stress–strain response for the $Ni_{50.7}Ti_{49.3}$ (at.%) sample under tensile loading. The specimen was loaded (under strain control) until 6% strain and unloaded (under stress control) to zero stress at 37 °C (body temperature). The response consists of the loading curve (path '1'–'2'–'3') followed by unloading curve (path '3'–'4'–'5'–'6'). During the loading, the stress increases up to 500 MPa within 0.8% strain (path '1'–'2') and continues with nearly constant stress until 6% strain at state '3'. In the unloading, the stress decreases rapidly from 500 MPa to 250 MPa within the small range of strain (path '3'–'4') followed by a nearly constant stress of 250 MPa while the strain decreases by a significant amount of nearly 4.5% (path '4'–'5'). Finally, the stress rapidly decreased to zero (path '5'–'6') showing a nearly complete recovery. Note that even in the simple case of a single load-unload isothermal cycle, there is still a slight deviation from the ideal condition of superelasticity, i.e., a small residual strain (between '6' and '1') at the end of the unloading does

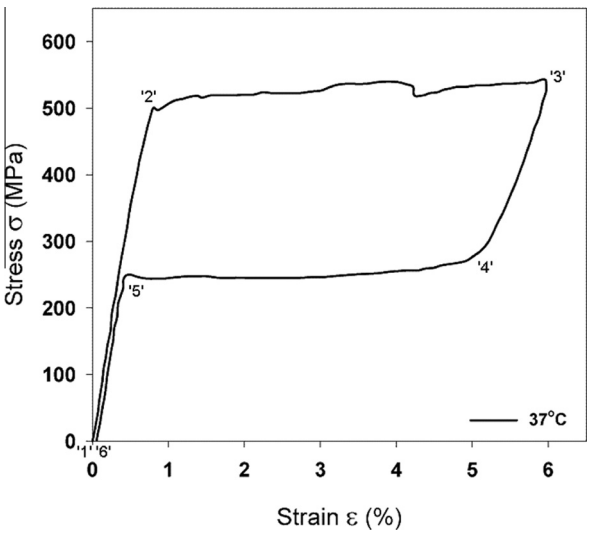

Fig. 5. Experimental stress-vs-strain response of the superelastic $Ni_{50.7}Ti_{49.3}$ at body temperature 37 °C, under combined control, i.e., strain control during loading to 6% and stress control to zero stress at end of the unload (Liu et al., 2008).

exist. It is interesting to note that even small changes in the amount of accumulated residual strain per cycle can amount to significant levels over many load-unload cycles, hence it is of great importance to studies connected to the phenomena of *functional fatigue* (Eggeler et al., 2004), which is especially important for many biomedical devices.

The test results in Fig. 5 shed light on the various stages exploited in the application of the self-expending stent mentioned above. For instance, the first loading stage ('1'–'2'–'3' in Fig. 5) is typical of the behavior that occurs while the stent is crushed for insertion into the catheter, whereas the behavior observed in the unloading stage ('3'–'4'–'5'–'6') determines the properties and behavior of the stent as it freely expands against the vessel wall during deployment.

2.5. The physical origin and macro–micro connection

Collectively, the macroscopic stress-vs-strain or strain-vs-temperature response curves described above are a manifestation of a rather complex array of micromechanical changes/phenomena occurring in the polycrystal upon applying mechanical and/or thermal loads. Chief among these are: (a) phase changes between the austenite (A) phase and different variants of the martensite (M) phase in each grain (crystal); (b) conversion of self-accommodated martensite to oriented/detwinned martensite variants under stress; and (c) a host of mutual grain-to-grain interaction and grain-boundary effects, etc. Note that for all the four materials considered here, the high-symmetry (A) phase is cubic B2, whereas the low-symmetry (M) variants are B19' monoclinic.

In this regard, reference is made to several of the available studies on the microstructure and texture of some of these polycrystalline materials. For an instance, the details of the microstructure for $Ni_{49.9}Ti_{50.1}$ and $Ni_{50.3}Ti_{29.7}Hf_{20}$ are available in the form of inverse pole figure (IPFs), and bright field transmission electron microscopy (BF-TEM) in Benafan et al. (2012) and Benafan et al. (2013), respectively. Similarly, results from the scanning electron microcopy (SEM), X-ray diffraction, and differential scanning calorimetry (DSC) are available for the PM/NiTi-P material in Krone et al. (2005). Furthermore, McNaney et al. (2003) presented the optical metallography and electron microscopy for superelastic NiTi. Note also that the above-mentioned references include further information regarding the processing utilized in obtaining the test specimens used for each of the four materials considered.

More specifically, starting with the simplest case of the tension test at 37 °C (higher than A_f = 19 °C) shown in Fig. 5 for the superelastic SMA material, one observes a forward A → detwinned M transformation along the path '1'–'2'–'3', where state '2' marks the critical/onset transformation stress. Upon unloading from state '3', the material undergoes reversed detwinned M → A transformation which is completed at state '6' with nearly full recovery of the strain accumulated during the loading stage.

Similarly, the same forward and backward phase transformation observed above also occurred in the isothermal tension test in the superelastic regime at 37 °C (higher than A_f = 29 °C) in Fig. 4(b) for the PM/NiTi-P material. On the other hand, a very different pseudoplastic response is observed in the case of isothermal tension test at −47 °C (lower than M_f = −43 °C), corresponding to the following micro-structural changes, i.e from self-accommodated, random-ordered variant M structure in the virgin state '1' to the oriented/detwinned M variant structure at state '3', where the strain reached 4% at the end of the loading stage. Finally, upon unloading to the zero stress state '4', the detwinned M structure continues to appear accompanied by a large amount of apparent residual strain.

With reference to the more elaborate test results of the cyclic isobaric tension experiments of Fig. 2(b) conducted on the $Ni_{49.9}Ti_{50.1}$ (at.%) material, the following remarks can be made. The virgin state '1' corresponds to the self-accommodated M structure (Benafan et al., 2013; Qiu, 2010). The test begins with an isothermal load-up stage at room temperature (path '1'–'2' in the Fig. 2(b)) to reach a predetermined bias-stress of magnitude 100 MPa, at which point a small amount (nearly 0.2%) of tensile strain was accumulated, comprised mainly of "elastic" deformation and a partial re-orientation of the M variants. This applied stress is held constant during the subsequent thermal cycling. The first transient thermal cycle starts at state '2' and contains the first heating and cooling branches '2'–'3' and '3'–'4', respectively. Particularly, during the heat branch '2'–'3', the partially oriented B19' martensitic structure undergoes the reverse transformation to the B2 austenitic structure. Note that no significant change in strain occurred during this first heating part. Subsequently, upon cooling through the forward transformation under constant stress (path '3'–'4' in the Fig. 2(b)), a large amount of strain occurs as the highly re-oriented B19' (M) structure is reached at state '4'. With increasing number of thermal cycles, a significant strain evolution occurs at the martensite and austenite states as can be seen in Fig. 2(b). At present, the details of the underlying micromechanical mechanisms leading to these strain evolutions are still not well understood. The occurrence of this unrecoverable strain has been attributed to many different mechanisms, such as transformation-induced plasticity, retained martensite, detwinned martensite, pinned residual martensite, austenite-martensitic interfaces, or dislocation slip etc. (Padula et al., 2012; Raj and Noebe, 2013; Goo et al., 1985; Belyaev et al., 2012; Pelton et al., 2012; Ezaz et al., 2013).

Conversely, the $Ni_{50.3}Ti_{29.7}Hf_{20}$ (at.%) material displays similar forward and reverse phase transformations to its $Ni_{49.9}Ti_{50.1}$ (at.%) counterpart. However, considering the isobaric cyclic behavior, $Ni_{50.3}Ti_{29.7}Hf_{20}$ (at.%) shows a low evolving characteristic $(\varepsilon_M^{(n)} - \varepsilon_M^{(1)})$ with increasing number of thermal cycles in comparison to the $Ni_{49.9}Ti_{50.1}$ (at.%) material. From the micromechanical point of view, the Hf and Ni-rich H-phase precipitates, which are formed during aging of the $Ni_{50.3}Ti_{29.7}Hf_{20}$ (at.%), are believed to play an important role for the thermo-mechanical cyclic stability of this material during isobaric, thermal cycling experiments. The reason behind the structural stability difference between $Ni_{50.3}Ti_{29.7}Hf_{20}$ (at.%) and $Ni_{49.9}Ti_{50.1}$ (at.%) lies in the occurrence of the H-phase precipitates which occurs in the $Ni_{50.3}Ti_{29.7}Hf_{20}$ (Yang et al., 2013) or lack thereof in the case of $Ni_{49.9}Ti_{50.1}$.

3. A general, 3D multi-mechanism SMA material model – summary

The SMA model developed by Saleeb et al. (2011) has targeted the modeling of both ordinary and high-temperature SMA materials. For many of the details of the mathematical formulation involved in this model, we refer the reader to the above mentioned reference. For our purpose here, we only give highlights of the main points pertinent to the parameterization of the four real SMA systems alluded to earlier in Section 2. In particular, several remarks are in order here regarding the formulation of the fundamental inelastic strain tensors and the associated viscoplastic formulation of the rate-dependent transformation strain. Rate dependency as observed in SMAs at different temperature regimes (pseudoelastic and pseudoplastic) has been attributed to different thermomechanical phenomena involved in the material's forward/backward transformation process. In particular, different reviews have been made in the SMA literature regarding the experimentally-observed diversity in the stress–strain responses of ordinary superelastic NiTi SMA wires subjected to different loading rates at high temperatures (>A_f). The variations in such responses/behaviors are partly due to differences in the magnitudes of latent heat generated and absorbed at the respective loading rates (Shaw and Kyriakides, 1995; and Grabe and Bruhns, 2008). Readers are referred to Lim and McDowell (1999) for comprehensive results showing the effect of strain rate on the behavior patterns of SMAs under different proportional and non-proportional load paths. Furthermore, detailed studies for the effect of wide variations in loading rates on the behavior of SMA materials at different temperatures are also available in Nemat-Nasser et al. (2005).

However, it is worth mentioning that other experimental investigations involving the same NiTi SMA material at temperatures lower than M_f, (where there is no likelihood of latent heat generation), show evidence of creep and relaxation at different loading and unloading stages where stress or strain is held constant for a period of time. The supporting evidence of the rate dependency of NiTi-based material systems in pseudoplastic (<M_f) and pseudoelastic (>A_f) regimes can be found Fig. 1 in Benafan et al. (2013) and Figs. 2.10 and 2.24 in Helm, 2001. Until further explorative studies are experimentally conducted to expound on the mechanisms responsible for "rate dependency" in SMAs, our model is formulated to accommodate applications in HTSMAs (where rate dependency is significantly determined by viscoplasticity at high temperatures) as well as ordinary SMAs. For our current study, however, the temperature is always treated as a controlled variable (hence, this will automatically account for any variation in measured temperatures due to latent heat generation and/or absorption). Furthermore, for all the considered characterization tests for the four SMA materials, the mechanical and/or thermal loadings are applied at moderate rates such that all factors which could account for rate effects are insignificant, hence the term "weak rate dependency" of the SMA materials.

The derivation of the constitutive equations used a Cartesian frame of reference and indicial notation. In the generalized 3D space, the total strain tensor is divided into elastic and inelastic parts. The strain tensor, ε_{ij} (and its rate $\dot{\varepsilon}_{ij}$) is a combination of ε^e_{ij} (reversible or elastic component) and ε^I_{ij} (irreversible or inelastic component). Tensor ε^I_{ij} is implicitly responsible for *all* transformation-induced deformations (forward/reverse transformations between A and M phases at higher temperature, detwinning of M-phase variants at lower temperature, as well as reorientations, variant coalescence and other allied effects under non-proportional states of stress and strain). The stress tensor, σ_{ij}, is decomposed into an effective stress, $(\sigma_{ij} - \alpha_{ij})$, and an internal state tensorial variable, $\alpha_{ij} = \sum_{b=1}^{N} \alpha_{ij}^{(b)}$, where N indicates the number of inelastic mechanisms. The stress-like, and conjugate strain-like, internal variables are denoted as $\alpha_{ij}^{(b)}$ and $\gamma_{ij}^{(b)}$, respectively, for $b = 1, 2, \ldots, N$ mechanisms. These internal variables regulate the energy storage ($b = 1, 2, 3$) and energy dissipations ($b = 4, 5 \ldots, N$) during the evolution of the thermomechanical response of the material. Based on the discussions in Saleeb et al. (2011), we have assumed here that $N = 6$.

The model formulation uses two fundamental *energy* potentials; i.e., a Gibb's complementary function, $\Phi = \Phi_R(\sigma_{ij}) + \Phi_{IR}\left(\sigma_{ij}, \alpha_{ij}^{(b)}\right)$, and a dissipation function, $\Omega\left((\sigma_{ij} - \alpha_{ij}), \alpha_{ij}^{(b)}\right)$, with the subscripts R and IR indicating reversible and irreversible(inelastic) components, respectively. Note that the parentheses above signify functional dependency. Following the procedure detailed in Saleeb et al. (2011), the resulting final equations in the model are summarized in Table 1 (basic equations) and Table 2 (transformations and hardening functions). Note also that the present SMA model accounts for large-deformation effects as described in Saleeb et al. (2013).

With regard to the material parameters needed in the mode used here, there are a total of 25 material parameters. For the elastic/reversible part of the model, an elastic modulus, 'E' and Poisson's ratio, 'υ' is used for each of the material systems. The remaining 23 parameters are devoted for the inelastic, non-linear part of the model. These include two sets: (1) parameters accounting for the inelastic/transformation strain (rate dependency factors, 'n' and 'μ'; threshold 'κ' in the transformation function; and distortion material parameters c, d), and (2) threshold values $\kappa_{(b)}$, and respective hardening rate parameters, i.e., modulus $H_{(b)}$ and exponent $\beta_{(b)}$ for mechanisms $b = 1$ to 6 in the evolution equations of the internal state variables. Note that the two material parameters (c, d) account for differences in the material deformation response under various loading modes, such as tension, compression, or shear, also referred to here as *intrinsic* asymmetry in tension and compression (ATC) parameters.

The above mentioned 25 (in total) material parameters can be further categorized into two groups: (1) 17 material parameters (E, υ, n, μ, d,$H_{(b)}$ and $\beta_{(b)}$ for $b = 1$ to 6) which are *fixed* and are not temperature/stress-state dependent, and (2) another set of 8 material parameters (κ, c, and $\kappa_{(b)}$ for $b = 1$ to 6) that account for the possible *temperature and/or stress-state dependencies* of the thermo-mechanical

Table 1
Summary of basic equations of the multimechanism SMA material model.

Equation set 1: decomposition of stress and strain

$\varepsilon_{ij} = \varepsilon^{e}_{ij} + \varepsilon^{I}_{ij}; \quad \alpha_{ij} = \sum_{b=1}^{N} \alpha^{(b)}_{ij}$

Equation set 2: specific functional forms for stored energy and dissipation potentials.

$\Phi_R(\sigma_{ij}) = \frac{1}{2}\sigma_{ij}\,\mathbf{E}^{-1}_{ijkl}\sigma_{kl}; \quad \Phi_{IR}\left(\sigma_{ij}, \alpha^{(b)}_{ij}\right) = \sigma_{ij}\varepsilon^{I}_{ij} + \sum_{b=1}^{N}\bar{H}_{(b)},$

$\Omega\left((\sigma_{ij} - \alpha_{ij}), \alpha^{(b)}_{ij}\right) = \int \frac{\kappa^2 F^n}{2\mu}\,\mathrm{d}F,$

Equation set 3: evolutionary laws

$\dot{\varepsilon}_{ij} - \dot{\varepsilon}^{I}_{ij} = \frac{\mathrm{d}}{\mathrm{d}t}\left(\frac{\partial \Phi_R}{\partial \sigma_{ij}}\right) = \mathbf{E}^{-1}_{ijkl}\dot{\sigma}_{kl}; \quad \dot{\varepsilon}^{I}_{ij} = \frac{\partial \Omega}{\partial \sigma_{ij}},$

$\dot{\alpha}^{(b)}_{kl} = \left[\frac{\partial^2 \Phi_{IR}}{\partial \alpha^{(b)}_{ij}\,\partial \alpha^{(b)}_{kl}}\right]^{-1} \dot{\gamma}^{(b)}_{ij}; \quad \dot{\gamma}^{(b)}_{ij} = -\frac{\partial \Omega}{\partial \alpha^{(b)}_{ij}},$

Where,

κ, μ and n are material constants, F is the transformation function and $\bar{H}_{(b)}$ are hardening functions (see Table 2).

E_{ijkl} is the isotropic fourth-order tensor of elastic moduli (Young's modulus, E and Poisson's ratio ν).

SMA responses such as strain evolution during thermal cycling, asymmetry in responses for tension, compression, and shear loading modes, and any other unique SMA behaviors.

4. Concurrent parameterization of the four SMA material systems

The calibration of the four material systems; superelastic $Ni_{50.7}Ti_{49.3}$, PM/NiTi-P, $Ni_{49.9}Ti_{50.1}$, and $Ni_{50.3}Ti_{29.7}Hf_{20}$ is carried out concurrently using the SMA model formulation (described in Section 3), based upon the complexity of the experimental thermomechanical response details for each material. Doing so demonstrates the ability of the general modeling approach to be exploited for any material system merely activating or deactivating the functional dependency of the different internal inelastic mechanisms.

Among the 17 fixed material parameters, some are maintained identical for all four SMA materials. These include the "handbook" value of Poisson's ratio, $\upsilon = 0.3$, as well as and the rate-dependency parameters, 'n', and, 'μ'. Here, since all four different SMA material classes considered are of the NiTi-based type, which is known to exhibit weak rate dependency in the temperature ranges considered for the test data used here (see Sections 2.1, 2.2, 2.3, 2.4), we have elected to use the *same* "large" value for 'n' and relatively "small value" for 'μ' in the calibration of *all* four materials ($n = 5$, and, $\mu = 10^5$ MPa s). In addition, the "deflated" elastic stiffness modulus, 'E' for each material system is assumed based on typical data available in the literature as mentioned in the tables given below for each material.

The key reference thresholds; κ in the transformation function, and $\kappa_{(b)}$ for mechanisms $b = 1$ to 6 and their respective hardening rate parameters $H_{(b)}$ and $\beta_{(b)}$ are required to be determined for each material system using the response of one base experimental test (see further details in Saleeb et al. (2011), Saleeb et al. (2013) and Saleeb et al., 2013). In the case of material systems requiring the temperature/stress dependency for the 7

Table 2
Summary of transformation and hardening functions used in the multi-mechanism SMA material model.

Equation set 4: transformation and hardening functions

$F(\sigma_{ij} - \alpha_{ij}) = \frac{1}{\kappa^2}\left[\frac{1}{2\rho^2}(\sigma_{ij} - \alpha_{ij})\mathscr{M}_{ijkl}(\sigma_{kl} - \alpha_{kl})\right],$

$\bar{H}_{(b)} = \begin{cases} \kappa^2_{(b)} \int \frac{1}{\bar{h}(g^{(b)})}\mathrm{d}G^{(b)}, & \text{for } b = 1,2,3; \\ \kappa^2_{(b)} \int \frac{1}{h(G^{(b)})}\mathrm{d}G^{(b)}, & \text{for } b \geqslant 4; \end{cases}$

$\bar{h}(g^{(b)}) = \begin{cases} \frac{\rho_{(b)}\kappa_{(b)}H_{(b)}\left(\sqrt{g^{(b)}}\right)^{\left(\beta_{(b)}-1\right)}}{\kappa_{(b)} + H_{(b)}\left(\sqrt{g^{(b)}}\right)^{\beta_{(b)}}}, & \text{for } b = 1,2, \\ \rho_{(b)}H_{(b)}\left[1 + \left(\frac{\sqrt{g^{(b)}}}{\kappa_{(b)}/H_{(b)}}\right)^{\beta_{(b)}}\right], & \text{for } b = 3, \end{cases}$

$h\left(G^{(b)}\right) = H_{(b)}\left[1 - \left(\frac{\sqrt{G^{(b)}}}{\rho_{(b)}}\right)^{\beta_{(b)}}\hat{h}(L)\right], \quad \text{for } b \geqslant 4;$

Where,

$G^{(b)}\left(\alpha^{(b)}_{ij}\right) = \frac{1}{2\kappa^2_{(b)}}\left(\alpha^{(b)}_{ij}\mathscr{M}_{ijkl}\alpha^{(b)}_{kl}\right); \quad g^{(b)}\left(\gamma^{(b)}_{ij}\right) = \gamma^{(b)}_{ij}\gamma^{(b)}_{ij}; \quad \rho = \frac{1 + c\sqrt{d}}{1 + c\sqrt{d + k_3}}; \quad \rho_{(b)} = 1$

$k_3 = \cos 3\theta$, where θ is Lode's angle calculated from the invariants of the effective stress $(\sigma_{ij} - \alpha_{ij})$. [Chen and Saleeb, 1994].

$\hat{h}(L)$ = the Heaviside function with argument being the loading index $L = \alpha^{(b)}_{ij}\Gamma_{ij}$; where

$\Gamma_{ij} = \partial F / \partial(\sigma_{ij} - \alpha_{ij})$.

$M_{ijkl} = \frac{1}{2}(\delta_{ik}\delta_{jl} + \delta_{il}\delta_{jk}) - \frac{1}{3}\delta_{ij}\delta_{kl}$; with δ_{ij} = Kronecker delta.

$H_{(b)}, \beta_{(b)}$, and $\kappa_{(b)}$ = material parameters for the individual hardening mechanism.

c, d = material parameters for tension/compression asymmetry [Saleeb et al., 2011]

key reference thresholds, the functional temperature/stress dependency will be expresses as $\kappa^{(\sigma_e)} = \kappa(T) \cdot \eta(\sigma_e)$ and $\kappa_{(b)}^{(\sigma_e)} = \kappa_{(b)}(T) \cdot \eta_{(b)}(\sigma_e)$; where T is the temperature, $\eta(or \eta_{(b)})$ is a non-dimensional factor that is dependent on the stress intensity only and the multi-axial stress intensity is defined as $\sigma_e = \sqrt{3(\sigma_{ij} \mathscr{M}_{ijkl} \sigma_{kl})/2}$. In such cases, tables will be provided for $\kappa(T), \kappa_{(b)}(T), \eta$ and $\eta_{(b)}$ as part of the calibration procedure.

4.1. $Ni_{49.9}Ti_{50.1}$ (at.%) SMA material

An extensive set of experimental results (see Section 2.1) for $Ni_{49.9}Ti_{50.1}$ under isobaric loading conditions at seven different bias stress levels (10, 50, 80, 100, 150, 200, and 300 MPa) for 100 thermal cycles using a temperature range of 30 °C to 165 °C were utilized for the SMA model calibration (for details see Saleeb et al. (2013) and Saleeb et al. (2013)). The calibrated parameters for $Ni_{49.9}Ti_{50.1}$ are presented in Table 3.

The fixed material parameters were calibrated from an isobaric test at 100 MPa (see upper part of Table 3). Any typical solid-state SMA actuator involves thermal cycling between the LCT < M_f and UCT > A_f. Thus, the test data for this SMA actuation material included thermal cycling between 30 °C to 165 °C under different constant stresses. Hence, the modeling feature of temperature/stress dependency for κ and $\kappa_{(b)}$ was activated in this material. This is achieved by selecting the values of characteristic regions of temperature changes labeled here as T1, T2, T3, and T4 as in the middle part of Table 3. Similarly, a number of characteristic values for stress changes were utilized to define the non-dimensional factors η and $\eta_{(b)}$ (see the last part of Table 3). Since only tensile, isobaric experimental results were available, the 2 material parameters (c, d) dealing with intrinsic tension/compression asymmetry are *not* active for this material. However, recall that the large-deformation effects will automatically produce some ATC effects depending on the magnitude of deformation.

4.2. $Ni_{50.3}Ti_{29.7}Hf_{20}$ (at.%) SMA material

An extensive experimental set of series isobaric tests for $Ni_{50.3}Ti_{29.7}Hf_{20}$ (see Section 2.2) under tensile bias stresses ranging from 0 to 500 MPa followed by compressive bias stresses ranging from 0 to 500 MPa, thermally cycled between 30 °C and 300 °C, were utilized for the parameterization of the present ternary SMA. The calibrated parameters for the $Ni_{50.3}Ti_{29.7}Hf_{20}$ SMA material are presented in Table 4.

As in Section 4.1, the values of the 17 fixed material parameters were determined from the strain-vs-temperature measurements at 100 MPa in tension in the above series test (see upper part in Table 4). Similarly, using the same part of the test data at the 100 MPa stress level, the temperature dependency of κ and $\kappa_{(b)}$ was handled through the choice of an appropriate set of the characteristic temperatures (T_1, T_2, T_3, T_4 and T_5) as explained earlier for the $Ni_{49.9}Ti_{50.1}$ material. The outcome of this procedure is depicted in the middle part of Table 4. Furthermore, utilizing the remaining strain-vs-temperature measurements at the other tensile bias-stress levels, i.e., for stress levels of 200, 300, 400 and 500 MPa, the stress dependency factors η and $\eta_{(b)}$ were evaluated as given in the middle part of Table 4.

To characterize the significant ATC effect observed in the test data of Fig. 3(b) for this material (for example, contrast the magnitudes of strain of 1.75% versus −1.08% measured at LCT at the end of the cooling branch of 2nd thermal cycle, and the actuation strokes of 1.5% versus −1.04% corresponding to the isobaric tensile and compressive tests at bias-stress value of 100 MPa, respectively), we have employed a constant value of 'd', together with the stress-dependent values of 'c' listed in the second column of the lower part of Table 4. These variations in the 'c' values were determined by comparing the compressive hysteresis loop versus their tensile counterparts.

Finally, the marked shifts in temperature of the transformation loops with bias-stress levels as measured in the test data of Fig. 3 (e.g., a shift of approximately positive 50 degrees when the stress magnitude changed from 100 MPa to 500 MPa either in tension or in compression) were simulated by the "temperatures-shift", T_{shift}, values given in the last column of the lower part of Table 4. In accordance with this, the functional temperature-dependency of $\kappa(T)$ and $\kappa_{(b)}(T)$ is simply replaced by $\kappa(T - T_{shift})$ and $\kappa_{(b)}(T - T_{shift})$, respectively. Note that these last two refinements in modeling (i.e., ATC and temperature-shift) were only needed for the present ternary material system.

4.3. A powder metallurgical processed NiTi SMA material

The powder metallurgical processed NiTi (P-NiTi) SMA material (see Section 2.3) was developed for the biomedical bone-stable application which exploits the one-way shape memory effect (OWSME) while heating from a temperature below M_f to above A_f (body temperature, i.e., 37 °C) under stress-free conditions. Ideally, isothermal tests conducted in both tension as well as compression at different temperatures should be available to enable the complete characterization of the bone staple SMA material, including the anticipated bending actions that can develop in different parts of the staple. However, *no* test data (Krone et al., 2005; Christ and Reese, 2009) was available regarding the compression behavior of this material. Therefore, the ATC aspects of the model were deactivated here. This leaves 23 material parameters to be determined for this case. The isothermal tensile stress-vs-strain test results available at 37 °C were utilized to obtain the 16 fixed material parameters, and the values for these are summarized in the upper part of Table 5. The isothermal tension tests at all available temperatures (−48 °C, 13 °C, 37 °C, 50 °C, and 90 °C) were subsequently utilized to determine the variation of κ and $\kappa_{(b)}$ with temperature. i.e., leading to the values of the characteristic temperatures $T1$, T_2, T_3, T_4 and T_5 as depicted in the lower part of Table 5. Note that all stress-dependencies are *deactivated* here, in view of the fact that the interest in the intended application involves OWSME under stress-free conditions.

4.4. A superelastic NiTi SMA material

This superelastic NiTi SMA material (see Section 2.4) is commercially available and is commonly used for the biomedical stent application which exploits the superelasticity property at a constant temperature above its A_f(body temperature, i.e., 37 °C). Thus, the calibration procedure ideally requires at least one isothermal tensile test and another compressive test at 37 °C. However, the available experiment (Liu et al., 2008) involved only a single loading/unloading tension cycle. Therefore, the ATC model refinement was *discarded* here.

In view of all the above combined factors, the calibration procedure in this case was significantly simplified. In particular, all temperature- and stress-dependencies are completely deactivated for this simple case. Consequently, the 23 material parameters in the model were taken to be fixed as shown in Table 6.

4.5. Further remarks and calibration guidelines

Considering the details of the parameterization/calibration exercise described above for the four different classes of the SMA materials (from Sections (4.1)–(4.4)), a number of important remarks are in order here. First, the degree of complexity of the calibration procedure depends upon the number and details of the experimental responses available and/or required for the SMA materials being used. For example, the parameterization of the superelastic NiTi for biomedical stent application was much simpler in contrast to that of the far more difficult cases involving NiTi-based actuation materials. Second, the key modeling ingredient in providing such calibration flexibility for different SMA systems is the convenient grouping of the material parameters into the fixed set (17 parameters) and the functionally-(temperature/stress) dependent set (maximum of 8 parameters). The degree of temperature and/or stress-state dependency to be utilized for these latter 8 material parameters determines the complexity of the parameterization.

Furthermore, Table 7 is presented to gain further insight into the level of difficulty required in the parameterization of each of the four SMA materials, thus providing a useful guideline for future use of the current modeling strategy for other material systems and their applications. In the one extreme, the parameterization of $Ni_{50.3}Ti_{29.7}Hf_{20}$SMA material is very complex, since in addition to the 17 fixed parameters, all the model refinements including the ATC, temperature-shift, as well as the *whole spectrum* of temperature/stress-dependencies for the 8 functionally dependent parameters needed to be *activated*. At the other extreme, the calibration of the superelastic NiTi material did *not*require any of the model refinements, thus rendering the calibration task very trivial with *fixed* values for *all* the needed 23 parameters. The parameterization of the remaining two SMA materials lies in between the above two extremes, as indicated by Table 7.

Finally, considering the specific nature of the temperature dependency alluded to above, very simple forms of this were used in the present work; i.e., piece-wise linear at most. Indeed, *not* all the potential variation of the 8 functionally dependent material parameters was utilized here to parameterize any of the four SMA materials. For example, even for the complex case of the 55NiTi ($Ni_{49.9}$-$Ti_{50.1}$) actuation material, it was only necessary to include the temperature-dependency of 5 parameters among the possible 8, whereas for both $Ni_{50.3}Ti_{29.7}Hf_{20}$ and PM/NiTi-P SMA materials, this was reduced further to only 3 temperature-dependent parameters. The simplest case of a superelastic $Ni_{50.7}Ti_{49.3}$ material did not require any temperature dependency. We view this flexibility in the choice of the functional dependency of some of the 8 material parameters in the present general modeling framework as a great practical utility in tackling future calibration tasks of new SMA systems.

4.6. Specific details for characterizing the powder metallurgical processed NiTi SMA material

For better understanding of the above general procedure for characterizing the model parameters, a detailed description of this procedure is outlined below for the specific example of the PM/NiTi-P SMA material. In this case we have 5 isothermal tests at different temperatures, with 2 of these tests including both loading as well as unloading measurements. Recall that for the present material, the characteristic transformation temperatures are $M_f = -43$ °C, $M_s = -23$ °C, $A_s = -13$ °C, and $A_f = 29$ °C. The results of these 5 tests have provided the guidance for the specific choices of the material parameters listed in Table 5. However, it is emphasized here that a number of model parameters i.e. $\upsilon = 0.3$, n = 5, and, $\mu = 10^5$ MPa s are assumed for the PM/NiTi-P SMA material (refer to the discussions relevant to these parameters in the general description at the beginning of the Section 4).

In particular, the following remarks are relevant in the specific extracting of the numerical values of the material parameters from the above-mentioned experimental results:

1. The material constant, E, was estimated based on the average of the slopes of the initial linear portion of the stress–strain curves of the available 5 tensile isothermal tests. Due to unavailability of the experiments on compression isothermal conditions, the parameters c, and$d$ accounting for ATC were made inactive with regards to the PM/NiTi-P SMA material. The readers are directed to Section 4.2, and also Saleeb et al. (2011), to view the capability of the SMA model to account for ATC effects in other material systems.
2. Estimation of the thresholds, $\kappa, \kappa_{(b)}, H_{(b)}$ and $\beta_{(b)}$ for mechanisms $b = 1$ to 6 were made using the experimental stress–strain curve at the 37 °C (>A_f), based on the guidelines outlined in Saleeb et al. (2011) and Saleeb et al. (2013). In particular, we have used this test at 37 °C (>A_f), since it is the only *pseudoelastic* experiment with *unloading* measurements.
3. The significant value of $\kappa_{(1)}$ and $\kappa_{(2)}$ in contrast to the very small value of $\kappa_{(4)}$ provided the level of transformation stress during the forward transformation (loading) and superelastic response during the reverse transformation (unloading) at such temperatures >A_f.

Table 3
Calibrated material parameters for $Ni_{49.9}Ti_{50.1}$ SMA material for actuation application.

Fixed material parameters							
Parameters	Units	Value					
E	MPa			60,000			
$H_{(b)}$ for b = 1 to 6	MPa	400×10^3	300×10^3	200	41×10^3	2×10^3	600
$\beta_{(b)}$ for b = 1 to 6	–	1	1	10	10	1	2.5
Temperature-dependency of material parameters κ and $\kappa_{(b)}$, for b = 1,2,. . .,6							
Temperature (°C)		Material parameters (MPa)					
		κ	$\kappa_{(b)}$, $b = 1,2$	$\kappa_{(b)}$, $b = 3$	$\kappa_{(b)}$, $b = 4$	$\kappa_{(b)}$, $b = 5$	$\kappa_{(b)}$, $b = 6$
T_1 = 20 °C		2	0.2	1.00E+21	130	10.875	52
T_2 = 65 °C (50 °C for b = 4)		20	0.2		0.01	21	
T_3 = 115 °C (120 °C for b = 4)		20	62.2		0.01	21	
T_4 = 200 °C		20	53.7		400	21	
Stress-dependency of the non-dimensional factors η and $\eta_{(b)}$							
Stress levels (MPa)		Scale factors					
		η	$\eta_{(b)}$, $b = 1,2$	$\eta_{(b)}$, $b = 3$	$\eta_{(b)}$, $b = 4$	$\eta_{(b)}$, $b = 5$	$\eta_{(b)}$, $b = 6$
10		0.070	0.125	1.000	1.000	0.900	0.100
50		0.150	0.500			1.206	0.304
80		0.600	0.800			1.200	0.700
100		1.000	1.000			1.000	1.000
150		1.300	1.500			1.667	1.500
200		2.350	1.950			1.400	2.500
300		4.000	2.700			6.667	3.000
375		10.000	3.450			22.833	5.872

Note: The intermediate values in the above table are interpolated linearly between the tabulated values.

Table 4
Calibrated material parameters for $Ni_{50.3}Ti_{29.7}Hf_{20}$ HTSMA material for actuation application.

Fixed material parameters							
Parameters	Units	Value					
E	MPa			75,000			
$H_{(b)}$ for b = 1 to 6	MPa	400×10^3	300×10^3	500	40×10^3	30×10^3	1800
$\beta_{(b)}$ for b = 1 to 6	–	1	1	1	1	1	5
Temperature-dependency of material parameters κ and $\kappa_{(b)}$, for b = 1,2,. . .,6							
Temperature (°C)		Material parameters (MPa)					
		κ	$\kappa_{(b)}$, $b = 1,2$	$\kappa_{(b)}$, $b = 3$	$\kappa_{(b)}$, $b = 4$	$\kappa_{(b)}$, $b = 5$	$\kappa_{(b)}$, $b = 6$
T_1 = 20 °C		40	0.1	16	256	20	1.00E+21
T_2 = 120 °C			0.1		0.01		
T_3 = 150 °C			0.1		0.01		
T_4 = 200 °C			320		64		
T_5 = 300 °C			320		64		
Stress-dependency of the non-dimensional factors η and $\eta_{(b)}$							
Stress levels (MPa)		Scale factors					
		η	$\eta_{(b)}$, $b = 1,2$	$\eta_{(b)}$, $b = 3$	$\eta_{(b)}$, $b = 4$	$\eta_{(b)}$, $b = 5$	$\eta_{(b)}$, $b = 6$
100		0.090	0.600	5.000	1.000	0.100	1.000
200		1.679	1.300	3.000		1.000	
300		2.949	2.000	1.000		1.000	
400		5.129	2.250	1.000		1.000	
500		6.994	2.500	1.000		1.000	
Stress-dependency of distortion constant c, d in transformation function and temperature-shift factor for transformation region							
Stress levels (MPa)		Distortion constants			Temperature-shift (in °C)		
		c	d				
100		0.56	1.05		−20.00		
200		0.48			−10.00		
300		0.45			0.00		
400		0.20			10.00		
500		0.20			20.00		

Note: The intermediate values in the above table are interpolated linearly between the tabulated values.

4. The parameters κ, together with *high* value of the modulus H5 and *significant*value for $\kappa_{(5)}$ (see column 5 in lower part of Table 5) are chosen to obtain the experimentally-observed *height* of the transformation loop.
5. The value of $\kappa_{(6)}$ is responsible for the cyclic characteristics of the material, hence the smaller $H_{(6)}$ and higher value of $\kappa_{(6)}$ together with an exponent $\beta_{(6)} = 1$ providing a larger strain range (estimated as $\kappa_{(6)}/H_{(6)}$) for possible evolution of the internal stress of this 6th mechanism. It is noted, however, that the lack of *cyclic* test data in the present exercise did not provide for a more precise estimation of the 3 parameters related to this 6th mechanism.
6. From the available 5 experimental stress–strain curves, the average limiting strain at which the forward phase transformation is completed (as indicated by a "rehardening" region following the shallow slope of the A → M transformation) is estimated to be approximately 5%. More specifically, to attain this in the model response, $\kappa_{(3)}$ and $H_{(3)}$ were selected such that the ratio, $\kappa_{(3)}/H_{(3)}$ will depict this rehardening strain of 5%. Furthermore, note the *high*value of $\beta_{(3)} = 5.5$ to enable the *rapidity* of evolution of the internal stress after 5% transformation strain.
7. The parameters κ and $\kappa_{(b)}$ for $b = 3, 5$, and 6 were maintained constant at *all* temperatures (see Table 5).
8. In order to capture the transition of the material response from the pseudoelastic regime (for $T > A_f$) to pseudoplasticity (for $T < M_f$), we utilized a temperature dependent variation for $\kappa_{(1)}$ and $\kappa_{(2)}$. More specifically, we utilized the following discrete values of 0.1, 78, 150,150 and 150 MPa at temperatures of −48 °C (no superelasticity), 13 °C (intermediate between A_s and A_f), 37 °C (significant superelasticity), 50 °C and 90 °C. It is interesting to note here that the test data for the two "superelastic" cases of 37 °C and 50 °C have indicated *identical* upper plateau maximum transformation stress (measured at ~2.5% strain), thus motivating us to assume the present *constant* values for $\kappa_{(1)}$ and $\kappa_{(2)}$ for the whole temperature ranging above 37 °C.
9. The estimated high values for the moduli $H_{(1)}$ and $H_{(2)}$ i.e. of the order of E, and the values for their corresponding $\beta_{(1)} = \beta_{(2)} = 1.8$ in Table 5 enabled us to obtain smoothly varying loading and unloading portions of the "flag-like" hysteresis loop near the zero-strain region of the case of 37 °C (as can be seen in Fig. 11(a) in Section 5.3 below).
10. Considering, the *pseudoplastic* response curve at −48 °C (<M_f), indicating a larger height of the hysteresis loop (compared to the test at 37 °C) and together with the fact that at this temperature there is no pseudoelasticity (i.e., negligible values of $\kappa_{(1)}$ and $\kappa_{(2)}$), we utilized a high value of $\kappa_{(4)}$ (see row 1 in lower part of Table 5) to account for the difference in the hysteresis loop height at −48 °C compared to the one at 37 °C.
11. Finally, to complete the temperature-dependency of $\kappa_{(4)}$, we considered the differences in the upper plateau stress (corresponding to 2.5% transformation strain during loading) at the different temperature cases (see Fig. 4(a) and (b) in Section 2.3 and also Fig. 11(a) and (b) in Section 5.3). In particular, we noted a much higher value for the upper plateau stress at 90 °C relative to the counterpart identical value at 37 °C and 50 °C. In order to account for these differences, we utilized $\kappa_{(4)}$ values of 0.01, 0.01, and 175 MPa at temperatures of 37 °C, 50 °C, and 90 °C, respectively as given in Table 5.
12. Because the way we are normalizing our modeling formulation (see Saleeb et al., 2011) and the distinct treatment of the dissipative mechanisms ($b = 4$ or higher) relatively to those storage mechanism ($b = 1$–3), the estimate for the saturated value for the uniaxial tension can be easily obtained from the threshold values $\kappa_{(b)}$ of mechanisms that will be saturated within the transformation range (i.e., approximately 2.5%). More specifically, in our present case involving uniaxial tension, using the values in Table 5 in the expression $\sqrt{3/2}\left(\sum_{b=1,2}\kappa_{(b)}^{saturated}\right)+\sqrt{3}\left(\kappa+\sum_{b\geq 4}\kappa_{(b)}^{saturated}\right)$, estimates for the upper plateau stress can be determined for the two cases of T = −48 °C and 37 °C. Therefore, the approximate upper plateau

Table 5
Calibrated material parameters for PM/NiTi-P SMA material for biomedical bone staple application.

Fixed material parameters							
Parameters	Units	Value					
E	MPa	90,000					
$H_{(b)}$ for b = 1 to 6	MPa	100×10^3	90×10^3	100	35×10^3	35×10^3	1150
$\beta_{(b)}$ for b = 1 to 6	–	1.8	1.8	5.5	1	1	1
Temperature-dependency of material parameters κ and $\kappa_{(b)}$, for b = 1,2,. . .,6:							
Temperature (°C)		Material parameters (MPa)					
		κ	$\kappa_{(b)}$, $b = 1, 2$	$\kappa_{(b)}$, $b = 3$	$\kappa_{(b)}$, $b = 4$	$\kappa_{(b)}$, $b = 5$	$\kappa_{(b)}$, $b = 6$
T_1 = −48 °C		20	0.1	5	52	15	50
T_2 = 13 °C			78		0.01		
T_3 = 37 °C			150		0.01		
T_4 = 50 °C			150		0.01		
T_5 = 90 °C			150		175		

Note: The intermediate values in the above table are interpolated linearly between the tabulated values.

Table 6
Calibrated material parameters for superelastic $Ni_{50.7}Ti_{49.3}$ SMA material for biomedical stent application.

Fixed material parameters							
Parameters	Units	Value					
E	MPa			90,000			
$H_{(b)}$ for b = 1 to 6	MPa	100×10^3	80×10^3	100	35×10^3	35×10^3	100
$\beta_{(b)}$ for b = 1 to 6	–	3	3	5	1	1	1
κ at 37 °C	MPa	12					
$\kappa_{(b)}$ for b = 1 to 6 at 37 °C	MPa	160	160	8	0.01	60	60

stress at 2.5% strain, for T = −48 °C and 37 °C can be evaluated as $0+\sqrt{3}(20+52+15) = 150.68$ MPa and $\sqrt{3/2}(150+150)+\sqrt{3}(20+0+15) = 428.05$ MPa, respectively (compare these stress values to the vertical stress reading in their respective experimental response in Fig. 4(a)). Starting with these estimates, the "fine tuning" of the model response curve to match the experiment is achieved from the remaining parameters.

13. As a corollary to item 12 above, Fig. 6 shows the intrinsic behavior of the individual mechanisms to achieve the respective pseudoplastic and pseudoelastic response at T = −48 °C and 37 °C as shown later in Fig. 11(a) of Section 5.3.

5. Assessments of calibrated model results

In this section, the calibrated model responses are compared to the experimental results of each individual SMA material to determine the performance and capability of the 3D multi-mechanism material model under different degrees of calibration. This investigation also validates the capability of the developed multi-mechanism SMA model to simulate all three different SMA features (i.e., superelasticity, pseudoplasticity and stress-assisted two-way SME). The following subsections show that the model predicts the material behavior with respect to the desired feature, regardless of the different levels of complexity used in the calibration of the four different materials. The calibrated material parameters for these four SMA materials, shown in Section 4, are utilized during the model simulations.

5.1. $Ni_{49.9}Ti_{50.1}$ (at.%) SMA material

During the calibration of this SMA material, an effort was made to capture the evolutionary response through thermal cycling. In the experimental results, two important typical features of the evolutionary response were observed. These are a marked transient change during the forward transformation through the first thermal cycle, followed by an ever diminishing evolutionary response leading to a nearly stabilized state.

The calibrated model was utilized to simulate the evolutionary response of the $Ni_{49.9}Ti_{50.1}$ (at.%) material in *seven* different isobaric tension tests conducted at 10, 50, 80, 100, 150, 200, and 300 MPa, with 100 thermal cycles between 30 °C and 165 °C for each (except in the 200 MPa case where test data was available for only 88 cycles). Fig. 7(a) and (b) show the strain-vs-temperature responses for 100 MPa obtained from the experimental case and its model simulation counterpart, respectively. The results clearly revealed that the experimental characteristics of the initial transient and evolutionary cyclic response were captured reasonably well by the SMA model. In particular, the transient characteristic which occurs during the initial loading and first thermal cycle was predicted reasonably well. Furthermore, the stages of evolutionary behavior, which consists of the early evolution between cycles 2 and 20, the intermediate evolution between cycles 20 and 50, and the approach to a nearly saturated state between the 50th and 100th cycles, were successfully captured.

To quantitatively compare the responses, the experimental and modeling strain values at martensite (ε_M), austenite (ε_A), and the actuation strains (ε_{ACT}) were

Table 7
The role of material-parameters grouping and activation-deactivation modeling features in handling the concurrent parameterizations of four SMA materials intended for widely-varying applications.

Model parameters	Material system			
	$Ni_{50.3}Ti_{29.7}Hf_{20}$	$Ni_{49.9}Ti_{50.1}$	Powder metallurgical NiTi	Superelastic NiTi
Fixed parameters	E, υ; n, μ, d; $H_{(b)}$, $\beta_{(b)}$ for b = 1–6	E, υ; n, μ; $H_{(b)}$,$\beta_{(b)}$ for b = 1–6	E, υ; n, μ, κ; $\kappa_{(b)}$ for b = 3, 5, and 6, $H_{(b)}$, $\beta_{(b)}$ for b = 1–6	E, υ; n, μ, κ; $\kappa_{(b)}$, $H(b)$, $\beta(b)$ for b = 1–6
Temperature-dependent thresholds parameters	$\kappa(b)$ for b = 1, 2, and 4	κ; $\kappa(b)$ for b = 1, 2, 4, and 5	$\kappa(b)$ for b = 1, 2, and 4	X
Stress-dependent thresholds parameters	κ; $\kappa(b)$ for b = 1, 2, 3, and 5	κ; $\kappa(b)$ for b = 1, 2, 5, and 6	X	X
ATC parameters	c (stress dependent)	X	X	X
T_{shift} parameter	stress dependent	X	X	X

Note: X = deactivated.
Elastic (standard/handbook) parameters: E, υ.
Flow and ATC parameters: n, μ, κ, c, d.
Hardening-mechanism parameters: $\kappa(b)$, $H(b)$ and $\beta(b)$ for b = 1 to 6.

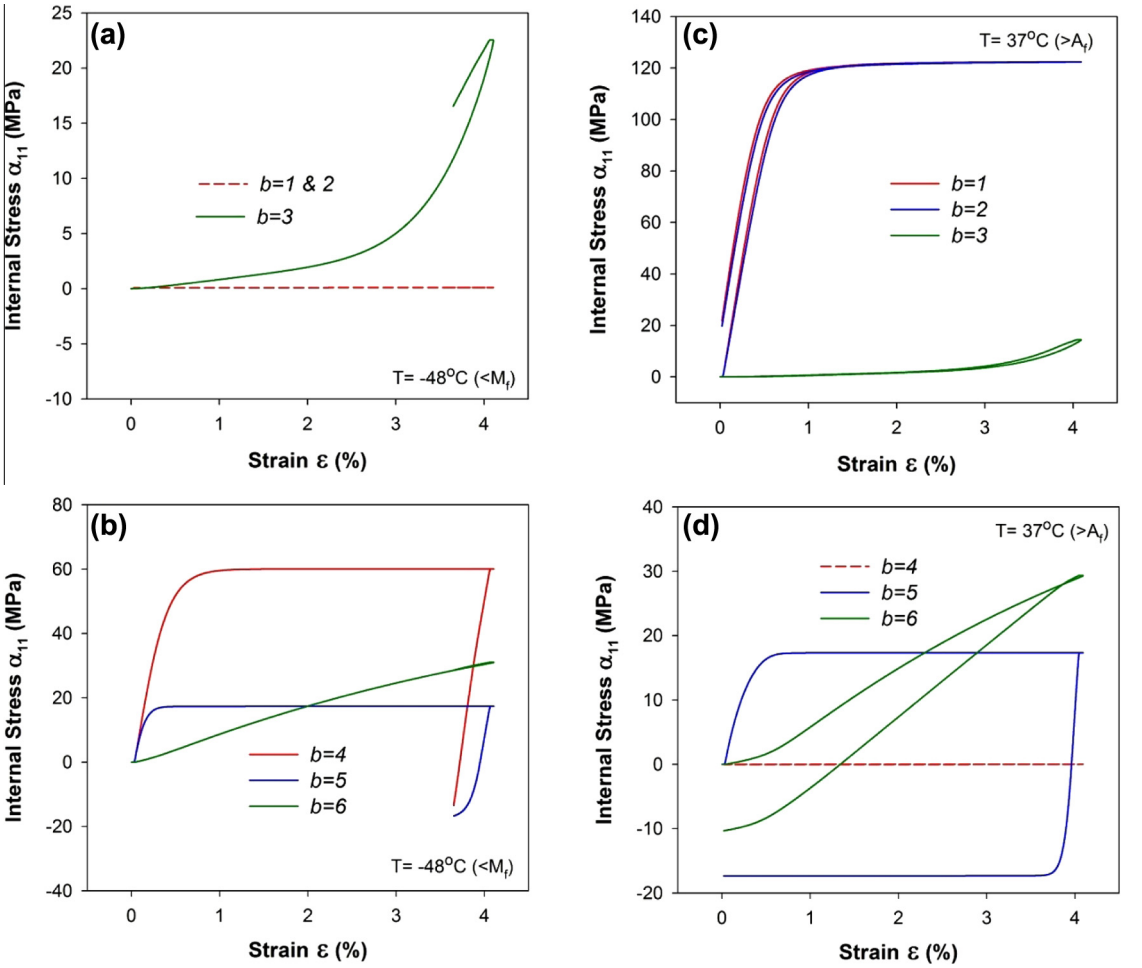

Fig. 6. Development of the first internal-stress component (where b = 1–3 for the storage inelastic mechanisms, and b = 4–6 for the dissipative mechanisms), with the tensile strain during the loading and unloading branches in the calibration of the powder metallurgical processed NiTi material. Parts (a) and (b) are for the test at T = −48 °C (<Mf) in the pseudoplastic regime, and parts (c) and (d) correspond to the pseudoelastic test at T = 37 °C (>Af).

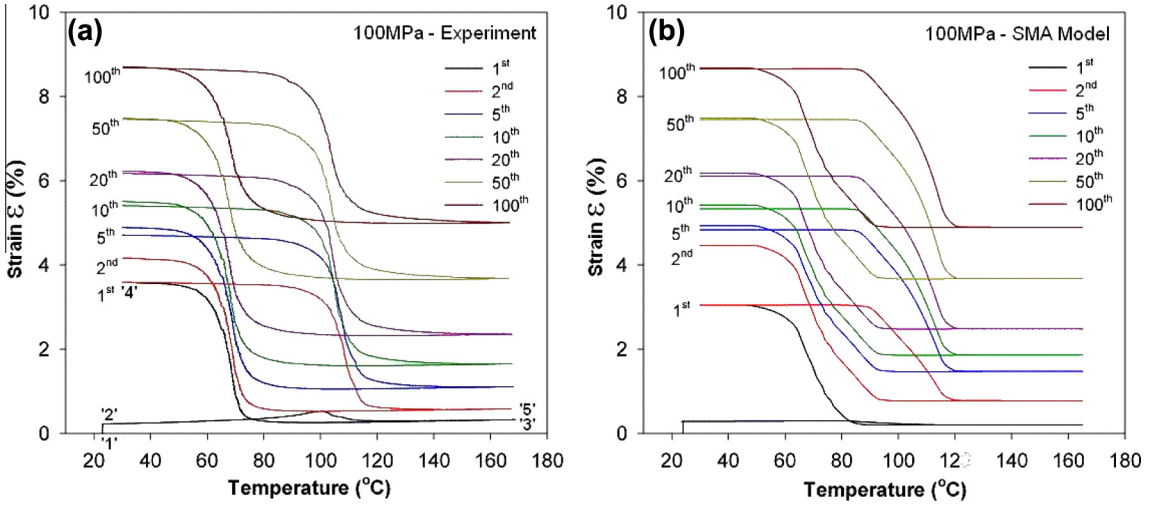

Fig. 7. Selected cyclic response (strain-vs-temperature response) at initial (1st, 2nd, and 5th) intermediate (10th, 20th to 50th) and later (50th to 100th) thermal cycles (100 cycles) for a isobaric test of $Ni_{49.9}Ti_{50.1}$: comparison of experimental and SMA model result, (a) 100 MPa- experimental and (b) 100 MPa-SMA model.

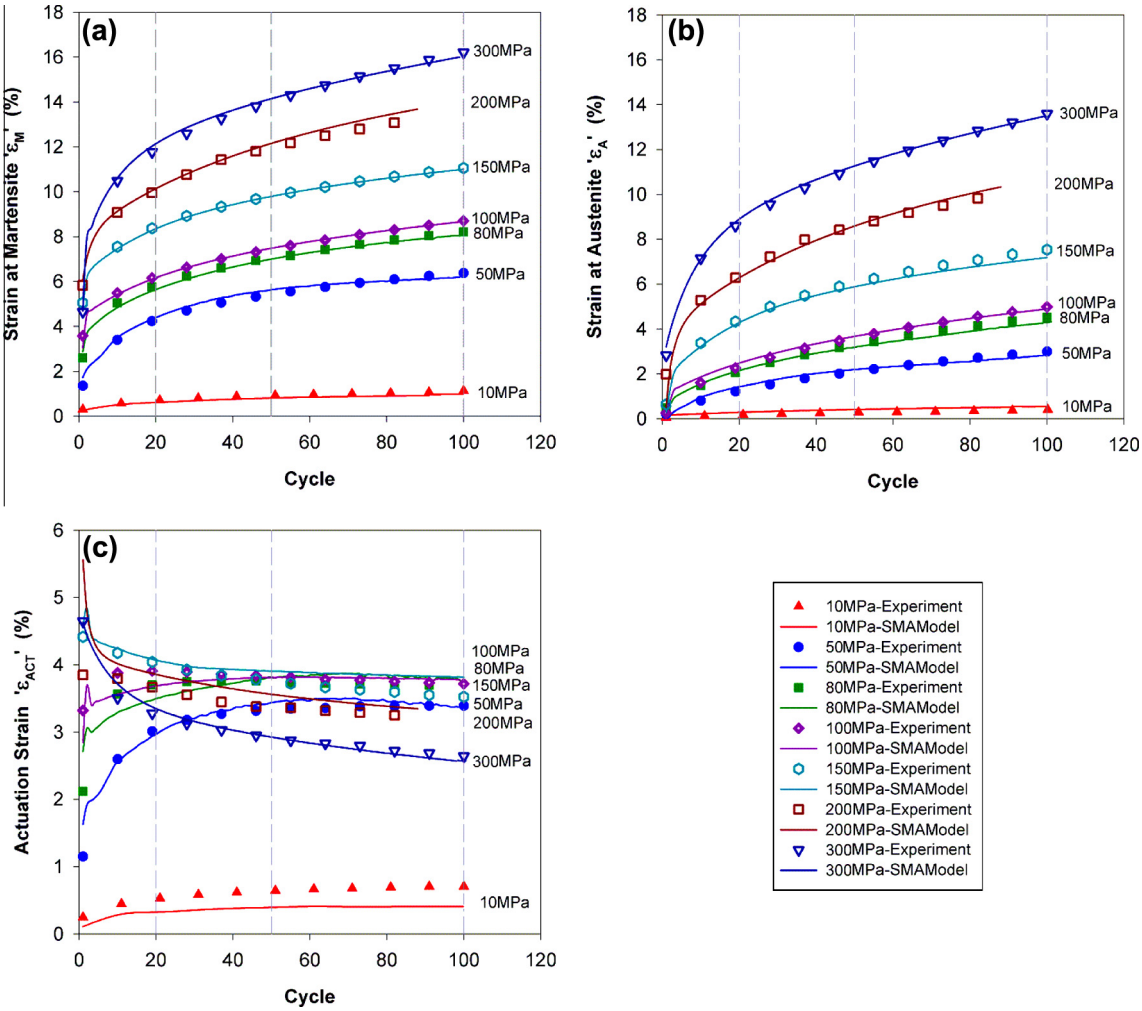

Fig. 8. Comparison of the experimental results with model counterparts for $Ni_{49.9}Ti_{50.1}$ at 10, 50, 80, 100, 150, 200, and 300 MPa for 100 cycles (except for 88 cycles for 200 MPa): (a) strain at martensite (ε_M), (b) strain at austenite (ε_A), and (c) actuation strain (ε_{ACT}).

superimposed as shown in Fig. 8(a)–(c). The detailed model results clearly revealed that strain evolution in the martensite (ε_M) and in the austenite (ε_A) increase non-linearly with an increasing number of thermal cycles, similar to their experimental counterparts. Note that the last cycles of each stage (early, intermediate evolutions and approach to nearly saturated state) are indicated by vertical dashed lines in Fig. 8(a)–(c). Moreover, the variation of the actuation strain in 100 thermal cycles displays a notable dependency on the applied stress. In terms of the range of the load-biased condition between 10 MPa and 300 MPa, the calibrated model successfully captured the stress dependency of the martensite strain (ε_M), austenite strain (ε_A), and the actuation strain (ε_{ACT}). Furthermore, the higher actuation strain reached at the stress value of about 100 MPa in the experiment was also successfully captured as shown in Fig. 8(c).

5.2. $Ni_{50.3}Ti_{29.7}Hf_{20}$ (at.%) SMA material

There are three important characteristics which were observed from the experimental response for the $Ni_{50.3}Ti_{29.7}Hf_{20}$ (at.%) material (Extrusion-124): (a) the effect of the *stress magnitude* on the corresponding transformation (actuation) strain, (b) a marked tension/compression *asymmetry*(ATC) in the response, and (c) a significant increase of the *transformation temperatures* with increasing stress. During the model calibration, the main effort was made to capture these specific characteristics of the $Ni_{50.3}Ti_{29.7}Hf_{20}$ (at.%) SMA material.

The model simulation was conducted using the same tension–compression experimental isobaric cases which were mentioned in Section 2.2 (see Fig. 3(b)). Qualitatively, the model was able to predict the overall pattern for each stress level as can be seen in Fig. 9(a) and (b). Note that the second thermal cycles are taken from the experiment and model results for each stress level. In particular, the underlying tension–compression asymmetry and the significant effect of the actuation strain resulting from changes of the bias-stress magnitude in both the tension and compression regimes were captured reasonably well by the SMA model.

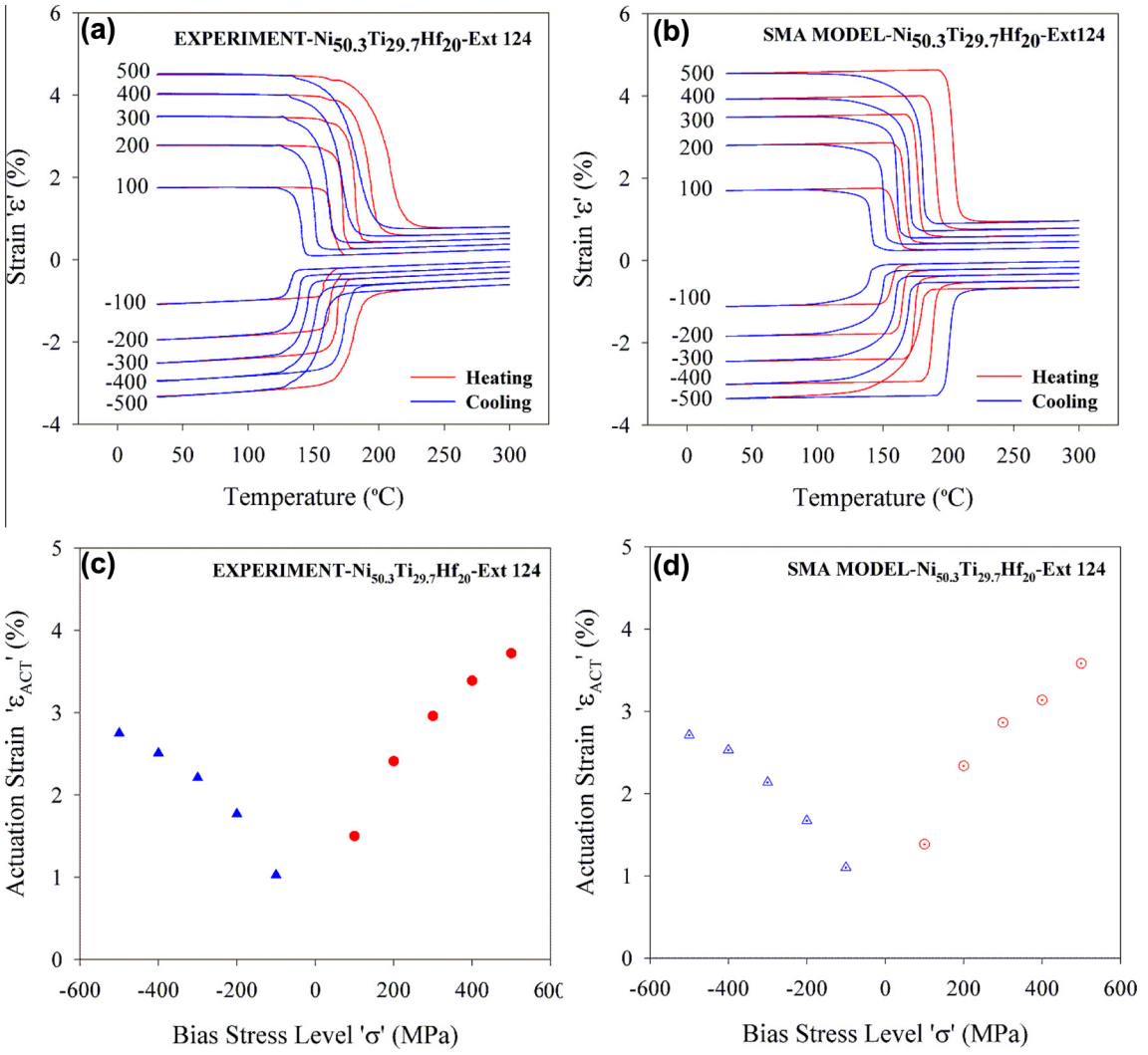

Fig. 9. Comparison of the experimental results with model counterparts for $Ni_{50.3}Ti_{29.7}Hf_{20}$ (Extrusion-124): (a) and (b): Cyclic response (2nd thermal cycle) for a series isobaric test between 30 °C and 300 °C at bias stress in tension (from 100 MPa to 500 MPa with increment of 100 MPa) followed by compression (from −100 MPa to −500 MPa with increment of −100 MPa): (a) experiment, and (b) SMA model. (c) and (d): Actuation strains at each stress levels in this test: (c) experiment, and (d) SMA model.

In order to acquire a detailed numerical comparison, the actuation strains (ε_{ACT}) were calculated and plotted against those from the experiments in Fig. 9(c) and (d). As can be seen from these figures, the SMA model was able to predict the actuation strain for the 2nd thermal cycle at five different bias stresses in the series isobaric test. In particular, the maximum actuation strain obtained in tension for the experimental and model results are 3.69% and 3.56%, respectively. Similarly, the maximum actuation strain in compression for the experimental and model results are 2.75% and 2.76%, respectively. It is important to note that the actuation strain increases with the bias-stress levels under both the tension and compression for this alloy. This suggests that higher actuation strains could be produced if higher bias-stresses were applied.

Likewise, as observed for the actuation strain in the experimental results, a marked transformation temperature asymmetry was also observed between the tensile and compressive deformation modes. Qualitatively, this temperature asymmetry was captured reasonably well by the model at each stress increment. In particular, the experimental and modeling results showed a gradual M_s temperature shift from 145 °C to 198 °C and from 145 °C to 191 °C, respectively (an ~50 °C change) as the stress increased from 100 to 500 MPa in tension. On the other hand, the compression results showed only an approximate 40 °C shift (from 138 °C to 175 °C in experiment result and from 145 °C to 185 °C in SMA model response), again highlighting the high stress sensitivity associated with this class of SMA material. Hence, combining the above observations regarding both the strain

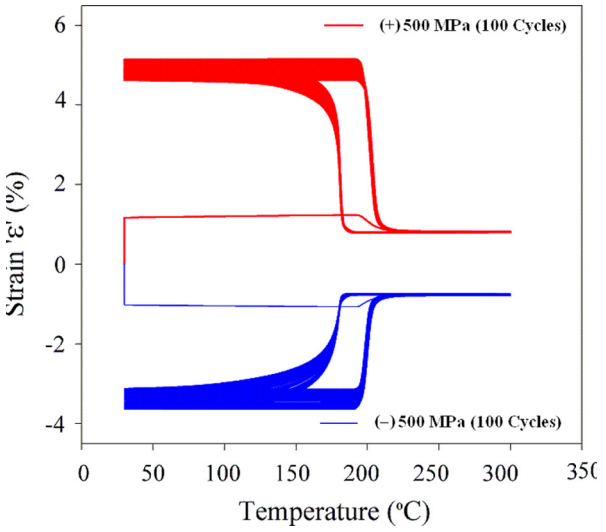

Fig. 10. Strain-vs-temperature model response of $Ni_{50.3}Ti_{29.7}Hf_{20}$ (Extrusion-124) for isobaric test at bias tensile (+) and compressive (−) stress of 500 MPa for 100 thermal cycles between 30 °C and 300 °C.

and temperature asymmetries make these materials extremely challenging to model.

Finally, on the basis of the assumptions made earlier in Section 2.2, the calibration of the SMA model for the $Ni_{50.3}Ti_{29.7}Hf_{20}$ (at.%) material (Extrusion-124) was carried out such that there is only relatively small magnitudes of strain evolution (over 100 thermal cycles at a given bias-stress) as observed in the case of Extrusion-146 (see Fig. 3). As a demonstration of this aspect, two isobaric tests were simulated under the bias tensile and compressive stress of magnitude 500 MPa for 100 thermal cycles between 30 °C to 300 °C, and the corresponding strain-temperature responses were plotted in Fig. 10. As can be seen from this figure, the accumulated strain during the evolution reached nearly 0.45% and 0.05% at the martensite (LCT) and austenite (UCT) sides, respectively, in each of the tension and compression cases.

5.3. A powder metallurgical processed NiTi SMA material

Unlike capturing only one type of material response (i.e., superelasticity or pseudoplasticity) some applications require both types of behaviors to be captured at different stages of operation. In such cases, several isothermal conditions must be considered during model calibration. For the PM/NiTi-P SMA material, two load-unload experiments and three loading only experiments at five different temperatures (−48 °C, 13 °C, 37 °C, 50 °C, and 90 °C) were used in the calibration. The experimental results and their SMA model counterparts are superimposed in Fig. 11(a) (for −48 °C and 37 °C) and Fig. 11(b) (for 13 °C, 50 °C, and 90 °C). Qualitatively, the results show that the calibrated model simulation successfully predicted each stress–strain response of the material at all five selected temperatures with negligible differences.

For the load-unload curves conducted to 4% strain followed by unloading (Fig.11)(a) and the experiments loaded to 5% strain (Fig. 11(b)), the model prediction coincides almost exactly with the experiments. More specifically, for the superelastic response at 37 °C, the end of the loading stage differs by only 3 MPa. For the pseudoplastic case (−48 °C), the end of the loading and unloading branches were captured perfectly by the model, indicating a significant residual strain (3.61%) after unloading. It is interesting to note that in the experiments conducted to 5% strain, the material demonstrates a rehardening behavior which is also well captured. In terms of the experimental and model results for the 13 °C and 50 °C cases, an excellent agreement was obtained for the linear elastic, stress plateau, and rehardening regimes of the deformation. However, a small deviation of the calibrated response from the experimental counterpart was observed at the onset of transformation for the isothermal test (load only) conducted at high temperature (90 °C).

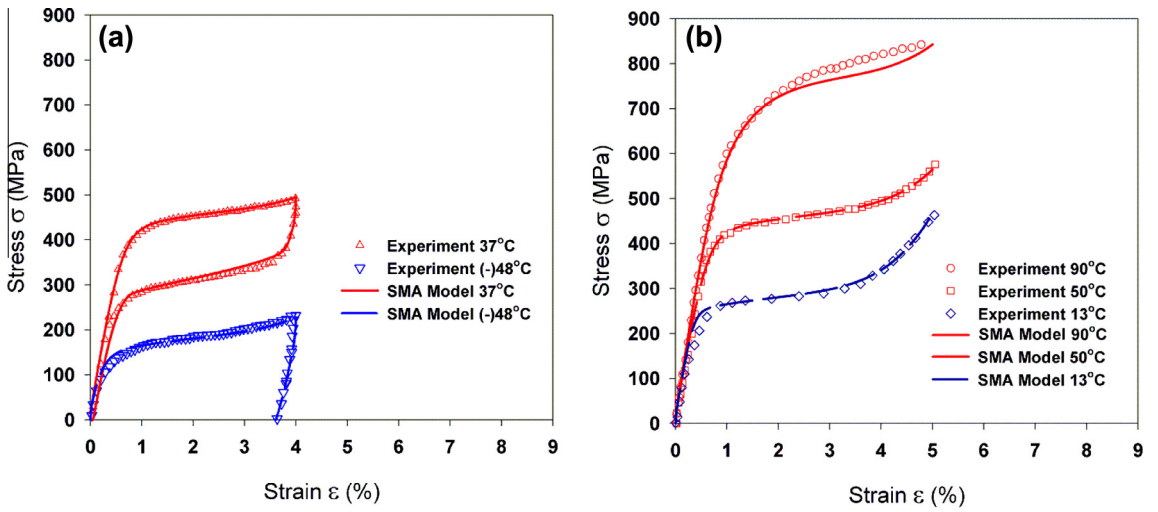

Fig. 11. Stress-vs-strain response for the powder metallurgically processed NiTi based SMA: comparison of experimental and SMA model result, (a) for load and unload at 37 °C and −48 °C and (b) for loading only at 90 °C, 50 °C, and 13 °C.

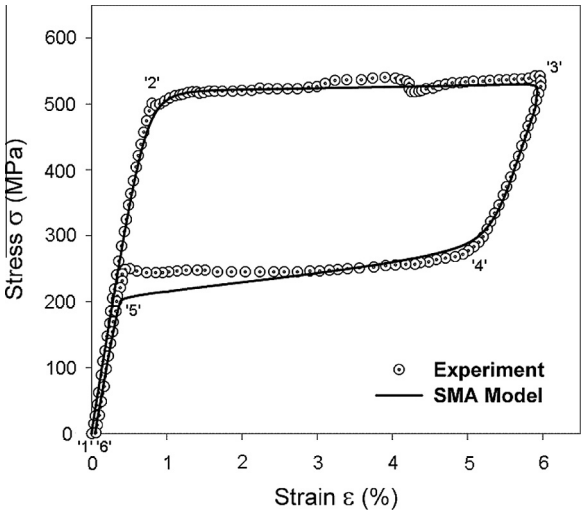

Fig. 12. Stress-vs-strain response of the superelastic NiTi SMA at body temperature 37 °C: comparison of experimental and SMA model result. Note that the experimental data in this figure was obtained from stable superelastic SMA wire.

5.4. A superelastic NiTi SMA material

The SMA model was used to predict the experimental results obtained from the $Ni_{50.7}Ti_{49.3}$ (at.%) SMA material, which exhibits superelastic characteristic at 37 °C (body temperature). The stress–strain curves comparing the experimental result with the model prediction were superimposed in Fig. 12 to better analyze the model's capabilities. Qualitatively, there is a good agreement between the experimental result and the model counterpart.

From the point of view of quantitative accuracy, the model successfully captured the initial steep increase in stress during the initial 0.8% strain increment (path '1'–'2') as well as the onset of the stress plateau at 500 MPa (path '2'–'3'). Indeed, almost all of the loading curve (path '1'–'2'–'3') lies directly on top of the experimental data, with only a 16 MPa difference at the end of the load-up. In the unloading branch, the rapid decrease in stress over the first 0.5% unloading strain (path '3'–'4') was also captured reasonably well. However, the lower stress plateau region (path '4'–'5') showed a gradual decrease until 200 MPa whereas the experimental curve exhibited a constant stress (250 MPa) until 0.5% strain. The widths of the energy dissipation areas for the experimental and model curves, which are measured from the middle of upper and lower stress plateaus, are 276 MPa and 281 MPa, respectively. Lastly, the final unloading branch (path '5'–'6') was captured with nearly complete strain recovery with residual of nearly 0.05%. Hence, despite a slight deviation in the unloading branch '4'–'5', the model was capable of accurately capturing the superelastic behavior of the $Ni_{50.7}Ti_{49.3}$ (at.%).

6. Conclusions

The present work focused on the concurrent parameterization of four different NiTi-based SMA material classes using a general, 3D, multi-mechanism, SMA material modeling framework. The choice of these specific material systems was motivated by two main considerations. First, two of the chosen materials (i.e., 55NiTi ($Ni_{49.9}Ti_{50.1}$) and superelastic $Ni_{50.7}Ti_{49.3}$) are among the most-widely used systems in applications and are commercially available, and the other two systems (i.e., ternary $Ni_{50.3}Ti_{29.7}Hf_{20}$ for aerospace applications and the powder metallurgically processed NiTi SMA system for biomedical applications) are representatives of research advances in material science for behavior enhancement. Second, the widely different response characteristics of the four SMA materials present an excellent setting to evaluate the robustness of the general framework.

To facilitate the task of model parameterization for each of the four SMA materials, a total of 25 involved material parameters were divided into two groups; i.e., 17 fixed parameters that govern the nonlinear hysteretic material response under any conditions of thermo-mechanical loading, and 8 material parameters which are devoted to handling the possible temperature and/or stress-state dependencies, thus enabling one to account for unique behaviors (i.e., refinements) such as evolution of strains with thermal cycles, asymmetry in response due to the differing loading modes (tension, compression, shear, etc).

The work presented has emphasized the viewpoint that the number and type of tests needed for proper parameterization/calibration is dependent on the types of technologically-significant applications for which a given material is targeted. In particular, the calibration effort varies depending on the complexity of the intended application. For instance, consider the *simple* task involved in the calibration of the superelastic NiTi for biomedical stent application, in contrast to the very *elaborate* calibration procedure required for the $Ni_{49.9}Ti_{50.1}$ and $Ni_{50.3}Ti_{29.7}Hf_{20}$, intended for solid-state actuation applications. This has guided the parameterization procedure utilized here which resulted in the finalized material parameter sets for the four SMA systems tabulated in Section 4.

In conclusion, and despite the great differences in the effort to obtain the model parameters for each of the four SMA materials, it is remarkable that these tabulated values of the model parameters proved to be very effective in predicting equally well all the experimentally observed thermo-mechanical responses. It is also worthy of note that these successful parameterizations for the four SMA materials were achieved despite the different nature of the test data utilized for each individual material, i.e., for a stable superelastic in Fig. 12 versus the virgin/ as-received/"untrained" cylindrical rod specimens for the cases of the actuation materials $Ni_{49.9}Ti_{50.1}$ and $Ni_{50.3}Ti_{29.7}Hf_{20}$ in Figs. 7–9, respectively.

Acknowledgments

This work was supported by NASA GRC, the Fundamental Aeronautics Program, Subsonic, Fixed-Wing, Project No. NNH10ZEA001N-SFW1, Grant No.: NNX11AI57A to the University of Akron. The authors would like to acknowledge Drs. S.M. Arnold and Ronald Noebe for their technical

guidance and programmatic support during the different phases of the project.

References

Angst, D.R., Thoma, P.E., Kao, M.Y., 1995. The effect of hafnium content on the transformation temperatures of Ni49Ti51– xHfx shape memory alloys. J. Phys. IV 5 (8), C8–747.

Atli, K.C., Franco, B.E., Karaman, I., Gaydosh, D., Noebe, R.D., 2013. Influence of crystallographic compatibility on residual strain of TiNi based shape memory alloys during thermo-mechanical cycling. Mater. Sci. Eng. A 574, 9–16.

Belyaev, S., Resnina, N., Sibirev, A., 2012. Peculiarities of residual strain accumulation during thermal cycling of TiNi alloy. J. Alloy Comput. 542, 37–42.

Benafan, O., Noebe, R.D., Padula II, S.A., Vaidyanathan, R., 2012. Microstructural response during isothermal and isobaric loading of a precipitation-strengthened Ni-29.7 Ti-20Hf high-temperature shape memory alloy. Metal. Mater. Trans. A 43 (12), 4539–4552.

Benafan, O., Noebe, R.D., Padula II, S.A., Gaydosh, D.J., Lerch, B.A., Garg, A., Bigelow, G.S., An, K., Vaidyanathan, R., 2013. Temperature-dependent behavior of a polycrystalline NiTi shape memory alloy around the transformation regime. Scr. Mater. 68 (8), 571–574.

Benafan, O., Noebe, R.D., Padula II, S.A., Garg, A., Clausen, B., Vogel, S., Vaidyanathan, R., 2013. Temperature dependent deformation of the B2 austenite phase of a NiTi shape memory alloy. Int. J. Plast. 51, 103–121.

Bigelow, G.S., Garg, A., Padula II, S.A., Gaydosha, D.J., Noebe, R.D., 2011. Load-biased shape-memory and superelastic properties of a precipitation strengthened high-temperature $Ni_{50.3}Ti_{29.7}Hf_{20}$ alloy. Scr. Mater. 64, 725–728.

Chen, W.F., Saleeb, A.F., 1994. Constitutive Equations for Engineering Materials, second revised ed. Elsevier, Amsterdam, New York.

Christ, D., Reese, S., 2009. A finite element model for shape memory alloys considering thermo-mechanical couplings at large strains. Int. J. Solids Struct. 46, 3694–3709.

Coughlin, D.R., Phillips, P.J., Bigelow, G.S., Garg, A., Noebe, R.D., Mills, M.J., 2012. Characterization of the microstructure and mechanical properties of a 50.3 Ni-29.7 Ti-20Hf shape memory alloy. Scr. Mater. 67 (1), 112–115.

Eggeler, G., Hornbogen, E., Yawny, A., Heckmann, A., Wagner, M., 2004. Structural and functional fatigue of NiTi shape memory alloys. Mater. Sci. Eng. A 378, 24–33.

Evirgen, A., Basner, F., Karaman, I., Noebe, R.D., Pons, J., Santamarta, R., 2012. Effect of aging on the martensitic transformation characteristics of a Ni-RICH NiTiHf high temperature shape memory alloy. Funct. Mater. Lett. 5 (04).

Ezaz, T., Wang, J., Sehitoglu, H., Maier, H.J., 2013. Plastic deformation of NiTi shape memory alloys. Acta Mater. 61, 67–78.

Gall, K., Tyber, J., Brice, V., Frick, C.P., Maier, H., Morgan, N., 2005. Tensile deformation of NiTi wires. J. Biomed. Mat. Res. Part A 75A (4), 810–823.

Goo, E., Duerig, T., Melton, K., Sinclair, R., 1985. Mechanical twinning in TiNiFe and TiNi alloys. Acta Metal. 33, 1725–1733.

Grabe, C., Bruhns, O.T., 2008. On the viscous and strain rate dependent behavior of polycrystalline NiTi. Int. J. Solids Struct. 45 (7–8), 1876–1895.

Hartl, D.J., Lagoudas, D.C., Calkins, F.T., Mabe, J.H., 2010. Use of a Ni60Ti shape memory alloy for active jet engine chevron application: I. Thermomechanical characterization. Smart Mater. Struct. 19, 015–020.

Helm, D., 2001. Formgedächtnislegierungen – experimentelle Untersuchung, phänomenologische Modellierung und numerische Simulation der thermomechanischen Materialeigenschaften (Ph.D. thesis), Universität Gesamthochschule Kassel.

Kan, Q., Kang, G., 2010. Constitutive model for uniaxial transformation ratcheting of super-elastic NiTi shape memory alloy at room temperature. Int. J. Plast. 26, 441–465.

Kockar, B., Karaman, I., Kim, J.I., Chumlyakov, Y., 2006. A method to enhance cyclic reversibility of NiTiHf high temperature shape memory alloys. Scr. Mater. 54, 2203–2208.

Krone, L., Mentz, J., Bram, M., Buchkremer, H.P., Stöver, D., Wagner, M., Eggeler, G., Christ, D., Reese, S., Bogdanski, D., Köller, M., Esenwein, S.A., Muhr, G., Prymak, O., Epple, M., 2005. The potential of powder metallurgy for the fabrication of biomaterials on the basis of nickel–titanium: a case study with a staple showing shape memory behaviour. Adv. Eng. Mater. 7, 613–619.

Lagoudas, D.C., Entchev, P.B., Popov, P., Patoor, E., Brinson, L.C., Gao, X., 2006. Shape memory alloys, part II: modeling of polycrystals. Mech. Mater. 38, 430–462.

Lim, T.J., McDowell, D.L., 1999. Mechanical behavior of an Ni–Ti shape memory alloy under axial-torsional proportional and nonproportional loading. J. Eng. Mater. Technol. 121 (1), 9–18.

Liu, X., Wang, Y., Yang, D., Qi, M., 2008. The effect of ageing treatment on shape-setting and superelasticity of a nitinol stent. Mater. Charact. 59, 402–406.

McNaney, J.M., Imbeni, V., Jung, Y., Papadopoulos, P., Ritchie, R.O., 2003. An experimental study of the superelastic effect in a shape-memory nitinol alloy under biaxial loading. Mech. Mater. 35 (10), 969–986.

Nemat-Nasser, S., Choi, J.-Y., Guo, W.-G., Isaacs, J.B., 2005. Very high strain-rate response of a NiTi shape-memory alloy. Mech. Mater. 37 (2–3), 287–298.

Noebe, R. 2012. Pitfalls and potential for developing stable high-temperature shape memory alloys through nano-precipitate strengthening. In: Proceedings, NASA Fundamental Aeronautics Program, Technical Conference, March 13–15, 2012, Cleveland, Ohio.

Otsuka, K., Wayman, C.M., 1998. Shape Memory Materials. Cambridge University Press, New York.

Padula II, S., Qiu, S., Gaydosh, D., Noebe, R., Bigelow, G., Garg, A., Vaidyanathan, R., 2012. Effect of upper-cycle temperature on the load-biased, strain-temperature response of NiTi. Metal. Mater. Trans. A 43 (12), 4610–4621.

Padula II, S.A., Gaydosh, D., Saleeb, A., Dhakal, B., 2013. Transients and evolution in NiTi. Exp. Mech., 1–7.

Patoor, E., Lagoudas, D.C., Entchev, P.B., Brinson, L.C., Gao, X., 2006. Shape memory alloys, part I: general properties and modeling of single crystals. Mech. Mater. 38, 391–429.

Pelton, A.R., Huang, G.H., Moine, P., Sinclair, R., 2012. Effects of thermal cycling on microstructure and properties in nitinol. Mater. Sci. Eng. A 532, 130–138.

Qiu, S., 2010. Investigation of thermal, elastic and load-biased transformation strains in NiTi shape memory alloys. Doctoral dissertation, University of Central Florida Orlando, Florida.

Raj, S.V., Noebe, R.D., 2013. Low temperature creep of hot-extruded near-stoichiometric NiTi shape memory alloy part II: effect of thermal cycling. Mater. Sci. Eng. A 581, 145–153.

Saleeb, A.F., Padula II, S.A., Kumar, A., 2011. A multi-axial, multi-mechanism based constitutive model for the comprehensive representation of the evolutionary response of SMAs under general thermo-mechanical loading conditions. Int. J. Plast. 27, 655–687.

Saleeb, A.F., Dhakal, B., Padula II, S.A., Gaydosh, D.J., 2013. Calibration of a 3D multi-mechanism SMA material model for the prediction of the cyclic attraction character in binary NiTi alloys. J. Intel. Mater. Syst. Struct. 24, 70–88.

Saleeb, A.F., Dhakal, B., Padula II, S.A., Gaydosh, D.J., 2013. Calibration of SMA material model for the prediction of the 'evolutionary' load-bias behavior under conditions of extended thermal cycling. Smart Mater. Struct. 22 (9), 094017.

Saleeb, A.F., Kumar, A., Padula II, S.A., Dhakal, B., 2013. The cyclic and evolutionary response to approach the attraction loops under stress controlled isothermal conditions for a multi-mechanism based multi-axial SMA model. Mech. Mater. 63, 21–47.

Shaw, J.A., Kyriakides, S., 1995. Thermomechanical aspects of NiTi. J. Mech. Phys. Solids 43 (8), 1243–1281.

Wada, K., Liu, Y., 2008. On the mechanisms of two-way memory effect and stress-assisted two-way memory effect in NiTi shape memory alloy. J. Alloys Compd. 449, 125–128.

Yang, F., Coughlin, D.R., Phillips, P.J., Yang, L., Devaraj, A., Kovarik, L., Noebe, R.D., Mills, M.J., 2013. Structure analysis of a precipitate phase in a Ni-rich high-temperature NiTiHf shape memory alloy. Acta Mater. 61, 3335–3346.

Yawny, A., Olbricht, J., Sade, M., Eggeler, G., 2008. Pseudoelastic cycling and ageing effects at ambient temperature in nanocrystalline Ni-rich NiTi wire. Mater. Sci. Eng. A 481–482, 86–90.